

DEEP NEAR-IR SURFACE PHOTOMETRY OF 57 GALAXIES IN THE LOCAL SPHERE OF INFLUENCE

EMMA M. KIRBY^{1,2} AND HELMUT JERJEN¹
Research School of Astronomy and Astrophysics,
Mt Stromlo Observatory, Australian National University,
Cotter Road, Weston ACT 2611, Australia

AND

STUART D. RYDER³
Anglo-Australian Observatory,
P.O. Box 296, Epping, NSW 1710, Australia

AND

SIMON P. DRIVER⁴
SUPA, School of Physics and Astronomy,
University of St. Andrews
Draft version June 2, 2021

ABSTRACT

We present H -band ($1.65\mu\text{m}$) surface photometry of 57 galaxies drawn from the Local Sphere of Influence (LSI) with distances of less than 10 Mpc from the Milky Way. The images with a typical surface brightness limit 4 mag fainter than 2MASS ($24.5\text{ mag arcsec}^{-2} < \mu_{lim} < 26\text{ mag arcsec}^{-2}$) have been obtained with IRIS2 on the 3.9 m Anglo-Australian Telescope. A total of 22 galaxies that remained previously undetected in the near-IR and potentially could have been genuinely young galaxies were found to have an old stellar population with a star density 1 – 2 magnitudes below the 2MASS detection threshold. The cleaned near-IR images reveal the morphology and extent of many of the galaxies for the first time. For all program galaxies, we derive radial luminosity profiles, ellipticities, and position angles, together with global parameters such as total magnitude, mean effective surface brightness and half-light radius. Our results show that 2MASS underestimates the total magnitude of galaxies with $\langle\mu_H\rangle_{eff}$ between 18 – 21 mag arcsec⁻² by up to 2.5 mag. The Sérsic parameters best describing the observed surface brightness profiles are also presented. Adopting accurate galaxy distances and a H -band mass-to-light ratio of $\Upsilon_*^H = 1.0 \pm 0.4$, the LSI galaxies are found to cover a stellar mass range of $5.6 < \log_{10}(\mathcal{M}_{stars}) < 11.1$. The results are discussed along with previously obtained optical data. Our sample of low luminosity galaxies is found to follow closely the optical-infrared B versus H luminosity relation defined by brighter galaxies with a slope of 1.14 ± 0.02 and scatter of 0.3 magnitudes. Finally we analyse the luminosity – surface brightness relation to determine an empirical mass-to-light ratio of $\Upsilon_*^H = 0.78 \pm 0.08$ for late-type galaxies in the H -band.

Subject headings: galaxies: dwarf – galaxies: stellar content – galaxies: fundamental parameters – galaxies: general – galaxies: photometry – infrared: galaxies

1. INTRODUCTION

The observational properties of nearby galaxies such as fluxes, colours, morphologies and sizes reflect their underlying physical properties (stellar/baryonic and dark matter content, star formation rates, formation history and angular momenta). Exactly how these observational and physical properties are related is still poorly understood. By technical necessity, the observational quantities are mainly based on the optical B -band (390 – 480 nm). However galaxies evolving in low density environments with little external stimulation for star formation often contain significant quantities of dust (eg. see Driver et al. 2007) which can attenuate and distort their optical light profiles. In contrast, dust attenuation is vastly reduced at near-IR wavelengths and hence the near-IR provides a spectral regime where a more accurate, unaltered representation of a galaxy’s underly-

ing stellar distribution can be obtained (Gavazzi et al. 1996b). Furthermore, the stellar mass of most galaxies is dominated by the quiescent old stellar component whose energy output peaks at near-IR wavelengths. Even in the extreme case of Blue Compact Dwarf (BCD) galaxies, previously thought to be primeval galaxies forming their first stars at the present epoch (Thuan & Izotov 1997), the analysis of their resolved stellar populations has revealed the presence of stars at least a few Gyrs of age (Schulte-Ladbeck et al. eg. the BCD galaxies: VII Zw 403, Mrk 178 and I Zw 36 as discussed by 1998, 2000, 2001, respectively; SBS 1415+437 discussed by Aloisi et al. 2005; I Zw 18 by Aloisi et al. 2007; and CGCG 269-049 by Corbin et al. 2008).

In order to obtain a deeper understanding of the connection between the light and matter distribution in galaxies, a representative sample of nearby stellar systems needs to be studied in detail. The Local Sphere of Influence (LSI, $D < 10$ Mpc) contains large numbers of early (dE) and late-type (dIrr) dwarf galaxies that make up about 85% of the local galaxy population (Kraan-

Electronic address: emma@mso.anu.edu.au, jerjen@mso.anu.edu.au
Electronic address: sdr@aao.gov.au
Electronic address: spd3@st-and.ac.uk

Korteweg & Tammann 1979; Schmidt & Boller 1992; Karachentsev et al. 2004). Dwarf galaxies contribute about 4% to the local luminosity density and about 10-15% to the local H I mass density (Karachentsev et al. 2004). Due to their proximity to the Milky Way, LSI galaxies are ideal for a near-IR study which includes significant numbers of dwarf systems.

Previous near-IR surveys include the Two Micron All Sky Survey (2MASS, Skrutskie et al. 2006) as well as deeper targeted galaxy surveys (Gavazzi et al. 1996a,c, 2000; Boselli et al. 2000). 2MASS photometry for galaxies suffers from a number of important drawbacks that are becoming more evident as the samples of independently investigated galaxies become larger. The short integration time of 2MASS observations resulted in most of the low surface brightness (LSB) dwarfs in the LSI remaining undetected, and if they were detected, 2MASS underestimated the fluxes by as much as 70% (Andreoni 2002). The targeted *H*-band observations of Gavazzi et al. (1996a,c, 2000) and Boselli et al. (2000) were inherently deeper however the samples included few LSB dwarfs. This serious limitation demands a deeper and higher resolution study to investigate those galaxies that were beyond the reach of photometric near-IR studies to date.

A reference atlas of images needs to have the necessary spatial resolution to probe the morphological fine-structure of these nearby galaxies and contain a significant number of dwarf galaxies that are generally overlooked. A LSI sample has the additional advantage that an increasingly large number of nearby galaxies have accurately known distances. Karachentsev et al. (2006) report that 214 out of 451 LSI galaxies have distance estimates (with less than 10% uncertainty) by means of the tip magnitude of the red giant branch (TRGB), the Tully-Fisher relation, and the surface brightness fluctuations (SBF) method (see for example Jerjen et al. 1998, 2001 and Karachentsev et al. 2004). The remaining galaxies have rough distance estimates from the luminosity of their brightest stars, radial velocities or their suspected membership to a known galaxy group.

The purpose of this paper is to present a near-IR *H*-band ($1.65\mu\text{m}$) atlas of 57 LSI galaxies, probing to flux levels approximately 4 mag arcsec⁻² or 40 times fainter than 2MASS. The majority of the galaxies presented here are much fainter than those in previous targeted surveys. We derive photometric parameters for each object such as the total magnitude, the effective radius and effective surface brightness, Sérsic fitting parameters, etc. Using the best distances currently available in the literature allows us to derive physical parameters such as their luminosities and stellar masses.

The paper is organised as follows: we describe the sample selection in §2. In §3 and §4 we discuss the observing strategies, the data reduction, and the photometric calibration of the images. The 11 galaxies in the sample which remained undetected at our faint detection limit or had images which could not be usefully analysed are discussed in §5. The new data is compared to 2MASS photometry and optical (*B*-band) data in §6 and the luminosity - surface brightness relation discussed. Interesting properties of individual galaxies are described in §7. Finally, the results are summarised in §8.

2. SAMPLE SELECTION

We have compiled a list of 470 galaxies with estimated distances less than 10 Mpc from the Milky Way¹, from the catalogues of Schmidt & Boller (1992), Côté et al. (1997), Jerjen et al. (2000), and Karachentsev et al. (2004). Approximately 70% of LSI galaxies are members of seven nearby galaxy groups including the Local Group (LG). Each group contains one or more massive spiral or elliptical galaxies accompanied by a population of dwarf satellites which tend to be dwarf ellipticals (dE). The southern hemisphere contains 174 LSI galaxies, 113 of which are members of a nearby group. We randomly selected 68 program galaxies with a range of total apparent *B*-band magnitude (between $m_B = 9$ and 18 mag, as well as several with no optical detection to date) and morphology (Hubble types E3 through to Sc, including many irregular and dwarf galaxies), 19 of which were members of a nearby group. Therefore, our sample contains 80% ($= \frac{68-19}{174-113}$) of southern hemisphere field galaxies and 17% ($= 19/113$) of group members. The distribution of these Local Sphere of Influence galaxies is shown in Figure 1.

The selected galaxies further provide a complementary data set to the Local Volume H I Survey (LVHIS; Koribalski 2007) which is a H I imaging survey of all LSI galaxies south of declination $\delta = -30^\circ$ that were detected by the H I Parkes All-Sky Survey (HIPASS, Barnes et al. 2001). The former H I survey is currently being carried out at the Australia Telescope Compact Array. The basic properties of our sample galaxies have been listed in Table 2 which is organised as follows:

Column (1). - Galaxy name.

Column (2). - Morphological type in the Hubble (1936), Sandage (1961), and Sandage & Binggeli (1984) classification scheme.

Columns (3) and (4). - Equatorial coordinates for the epoch J2000.

Column (5). - Total *B*-band magnitude and its source. When the uncertainty associated with this value is not provided, an error of 0.2 mag has been adopted.

Columns (6) and (7) - Distance to the galaxy (from Karachentsev et al. 2004, 2006; Seth et al. 2005; Carrasco et al. 2001) with an indication of the method used: (TRGB) tip magnitude of the red giant branch; (SBF) surface brightness fluctuations; (MEM) group membership; (H) Hubble flow distance $D = v_{LG}/H_0$ where $H_0 = 73 \text{ km s}^{-1} \text{ Mpc}^{-1}$ is adopted (WMAP, Spergel et al. 2007).

Column (8). - Heliocentric radial velocity, v_\odot , from the NASA Extragalactic Database (NED).

¹ Note that five galaxies have had their distance estimates revised since their inclusion in the sample and have a distance greater than 10 Mpc.

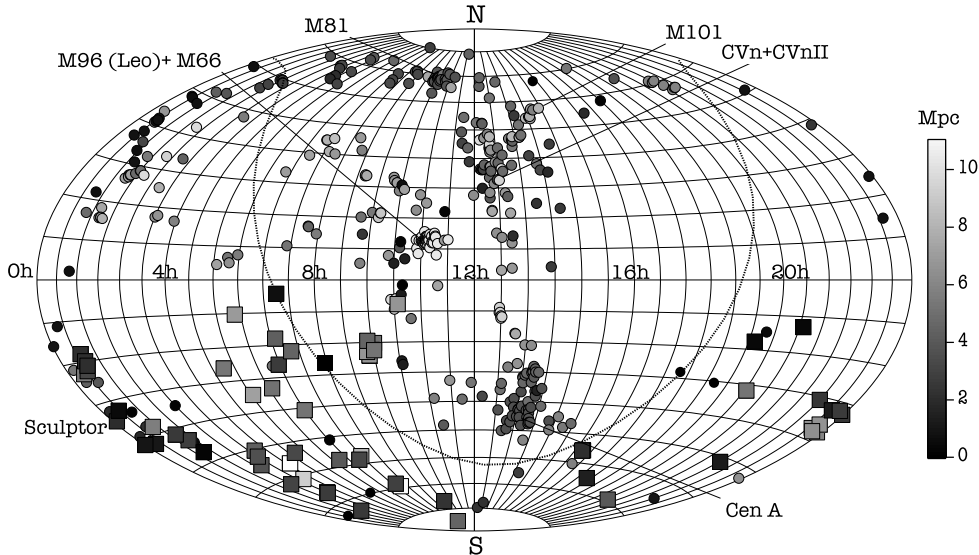


FIG. 1.— The distribution of galaxies within the Local Sphere of Influence. The circles represent the 451 galaxies listed in Karachentsev et al. (2004) plus 19 from other catalogues, and the squares are the 68 galaxies investigated in our study. The greyscale reflects a galaxy’s distance. The curved line shows the location of the Galactic plane.

Column (9). - Local Group velocity, v_{LG} , from NED.

Column (10). - Reddening estimate, $E(B-V)$ from Schlegel et al. (1998). The associated error is 16%.

Columns (11), (12), (13) and (14). - The observing log. The observation date, strategy, total exposure time and seeing is listed.

3. OBSERVATIONS AND REDUCTION

Near-infrared H -band images were obtained for the 68 program galaxies during five observing runs between October 2004 and September 2006, using the Infrared Imager and Spectrograph 2 (IRIS2; Tinney et al. 2004) at the 3.9 m Anglo-Australian Telescope (AAT) by the 3.9 m Anglo-Australian Telescope (AAT). Table 2 lists the observing log of the observations. Atmospheric conditions were clear if not always photometric, and the seeing ranged from $1''.0$ to $2''.9$ with a mean of $1''.3$. The IRIS2 detector is a 1024×1024 Rockwell HAWAII-1 HgCdTe array with a pixel scale of $0''.45 \text{ pixel}^{-1}$, resulting in an instantaneous field-of-view (FoV) of $7'.7 \times 7'.7$.

Two different observing strategies were employed, depending on the anticipated angular extent of the target compared to the IRIS2 FoV:

- **JITTER SELF FLAT (JSF)** – The majority of our sample have optical diameters $< 2'$ and, given the sky is typically $7 - 8 \text{ mag arcsec}^{-2}$ brighter in the H -band than the B -band, we anticipate these objects filling barely 10 – 20% of the array in the infrared. These targets were observed in a 3×3 grid pattern with a spacing of $90''$, resulting in a $4'.7 \times 4'.7$ overlap region common to all pointings that encompasses not just the target galaxy but also a substantial amount of the background sky. A maximum of ~ 30 seconds was spent on any one pointing, consisting of multiple 5–10 s integrations (depending on the sky brightness at the time while

aiming to keep the combined object + sky counts well within the linear regime) which were then averaged before being stored. This 9-point jitter pattern was repeated up to 6 times, leading to a total on-source exposure time of just under half an hour per galaxy. This method was also employed on larger, but well-resolved targets such as the Argo Dwarf Irregular galaxy.

- **CHOP SKY JITTER (CSJ)** – In accordance with the recommendations of Vaduvescu & McCall (2004), objects filling $\gtrsim 40\%$ of the array FoV require matching observations of adjacent blank sky to track changes in the background level and illumination pattern. Five jittered observations ($10''$ offsets) of the target galaxy were bracketed and interleaved with six jittered observations of the (relatively blank) sky $10'$ north or south. At each object or sky jitter position, $3 \times 10 \text{ s}$ or $6 \times 5 \text{ s}$ integrations were averaged. This pattern was repeated between 5 and 12 times, for a total on-source exposure time of up to half an hour per galaxy.

The data reduction was carried out using the ORAC-DR² pipeline within the STARLINK package. Observations made with the JSF method employed the JITTER_SELF_FLAT recipe, while those with the CSJ method used the CHOP_SKY_JITTER recipe. Pre-processing of all raw frames included subtraction of a matching dark frame; linearity and inter-quadrant crosstalk correction; and bad pixel masking.

Considerable care was taken to ensure accurate flat-fielding over the entire field of the array. For JSF observations, an interim flatfield is created by taking the median at each pixel of the nine normalised object frames, then each of the nine images is divided by this interim

² <http://www.oracdr.org/>

flatfield. Extended sources within these flatfielded object frames are automatically detected and masked, and an improved flatfield created from masked versions of the nine normalised object frames. A correction for astrometric distortion internal to IRIS2 is applied by re-sampling the properly flatfielded images, then spatial additive offsets between images are computed using point sources common to all images. The nine images are mosaiced together by applying offsets in intensity to the registered images to produce the most consistent sky value possible in the overlap regions. A new flatfield and mosaic is constructed for each set of nine jittered frames, then all the mosaics registered and co-added to form a master mosaic. Occasionally, significant variations in the level and/or structure of the background sky on a temporal or spatial scale smaller than that sampled by the array within the ~ 5 minute period of the nine jittered frames resulted in noticeable residual structure in the ensuing mosaic, forcing us to exclude that mosaic from the master mosaic. The total on-source exposure time, after discarding such data, is shown in Table 2.

For CSJ observations, the six sky frames are first offset in intensity to a common modal value, then a flatfield formed from the median value at each pixel. All six sky frames, and five object frames are flatfielded, then the modal pixel values of the two sky frames bracketing each object frame are averaged and subtracted from that object frame. Image registration and mosaicing is then performed on each set of five sky-subtracted object frames just as for the JSF observations. These mosaics are registered and co-added to form a master mosaic, with the exception of any showing residual sky structure as described above, yielding the on-source exposure times shown in Table 2.

Of the 68 galaxies observed, 11 remained undetected or could not be usefully analysed. This was either because our H -band surface brightness limit of $\mu_{lim} \approx 25 \text{ mag arcsec}^{-2}$ or $20 L_{\odot} \text{ arcsec}^{-2}$ at a distance of 1 Mpc (adopting $M_{H,\odot} = 3.35 \text{ mag}$, Colina et al. 1996) was not low enough or the galaxy light was heavily contaminated by Galactic foreground stars (see Table 1). In both situations the data was not processed further. For instance, the companion galaxies NGC2784 DW1 and KK98-73 were observed parallel to NGC2784. While NGC2784 and KK98-73 can be seen, NGC2784 DW1, located between NGC2784 and KK98-73, is barely visible (see Figure 5, second row, middle panel where KK98-73 is visible to the bottom left of the image). The images of the other 57 galaxies are shown in Figures 2 to 6.

On each image, instrumental magnitudes for 50–100 field stars were measured employing standard IRAF PSF fitting routines. Cross-correlating the stellar positions with the 2MASS Point Source Catalog provided H -band magnitudes and allowed the photometric calibration of each field (see Figure 7). The stars which deviate from the 45 degree line were usually either extremely red or blue where the transformation between 2MASS and IRIS2 H -bands (Ryder 2007) breaks down. The 1σ uncertainty in the zero point was calculated to be between 0.01 and 0.04 mag depending on the number of stars used for the calibration.

To ensure accurate galaxy surface photometry down to the faintest possible isophotes, the images were cleaned of foreground stars using procedures written within the

IRAF package. Thereby, stars in the field around a galaxy were carefully replaced with nearby patches of plain sky. If superposed on the galaxy, the galaxy light under the star was restored by replacing the contaminated area with its mirror image with respect to the galaxy center. The galaxy center was defined as the center of the luminosity-weighted light distribution. The star removal process was monitored visually to identify small-scale structures and asymmetries, and to ensure accurate removal of foreground stars whilst not removing sources associated with the galaxy itself. The effectiveness of the cleaning procedure is illustrated in Figure 8 where pre- and post- cleaning images are shown for the two galaxies ESO468-G020 and IC1959.

The fields of IC5152 (Figure 4) and UGCA438 (Figure 6) both have a bright foreground star which obscures a large portion of the galaxy. To obtain rough photometric parameters for these objects, the contribution of the bright stars to the total flux needed to be removed. Because such a large portion of both the galaxies is obscured, it was necessary to remove the affected quarter of the image and replace it with the opposite quarter, which was rotated by 180 degrees (i.e., in the case of IC5152, the top-right quarter was replaced with the rotated bottom-left quarter of the image). This method failed in the case of the dIrr galaxy AM0521-343, where an even brighter star (CD-34 2225, $m_H = 7.1$) near the faint dwarf galaxy prevented proper cleaning (see Figure 2).

4. SURFACE PHOTOMETRY

Simulated circular aperture photometry of the star-subtracted H -band images produced a growth curve as a function of the geometric mean radius \sqrt{ab} (where a and b are the galaxy's major and minor axes). The asymptotic intensity corresponds to the total apparent magnitude, m_H , that can be recovered down to the background noise level of the image. The largest source of uncertainty is the sky level. By systematically varying the sky brightness we determined which growth curve converges best to a plateau as far as possible from the center of the galaxy. We measure the half-light geometric mean radius, r_{eff} , at half the asymptotic intensity and calculated the mean surface brightness within that radius: $\langle\mu_H\rangle_{eff}$. The overall uncertainty for the total magnitude, m_H , is between 0.05 and 0.30 mag; for the mean effective surface brightness, $\langle\mu_H\rangle_{eff}$, less than $0.2 \text{ mag arcsec}^{-2}$, and for the half-light radius, r_{eff} , is of the order of five percent. The image of AM0521-343 (Figure 2), contains a bright foreground star and thus, the sky brightness plus the contribution from the stellar halo was estimated at the galaxy's position and simulated aperture photometry performed out to the radius of asymptotic intensity (defined on side of the galaxy opposite to the contaminating star).

The radial surface brightness profile of a sample galaxy was determined by differentiating the growth curves with respect to radius. Depending on the total integration time of the image, the profiles could be reconstructed down to a surface brightness limit between $24.5 \text{ mag arcsec}^{-2} < \mu_{lim} < 26 \text{ mag arcsec}^{-2}$. They are shown, with a linear radius scale in Figures 9, 10 and 11. The error bars are calculated as the rms scatter of the intensity along each isophote. The position angle and ellipticity for each isophote, with the galaxy center fixed, were

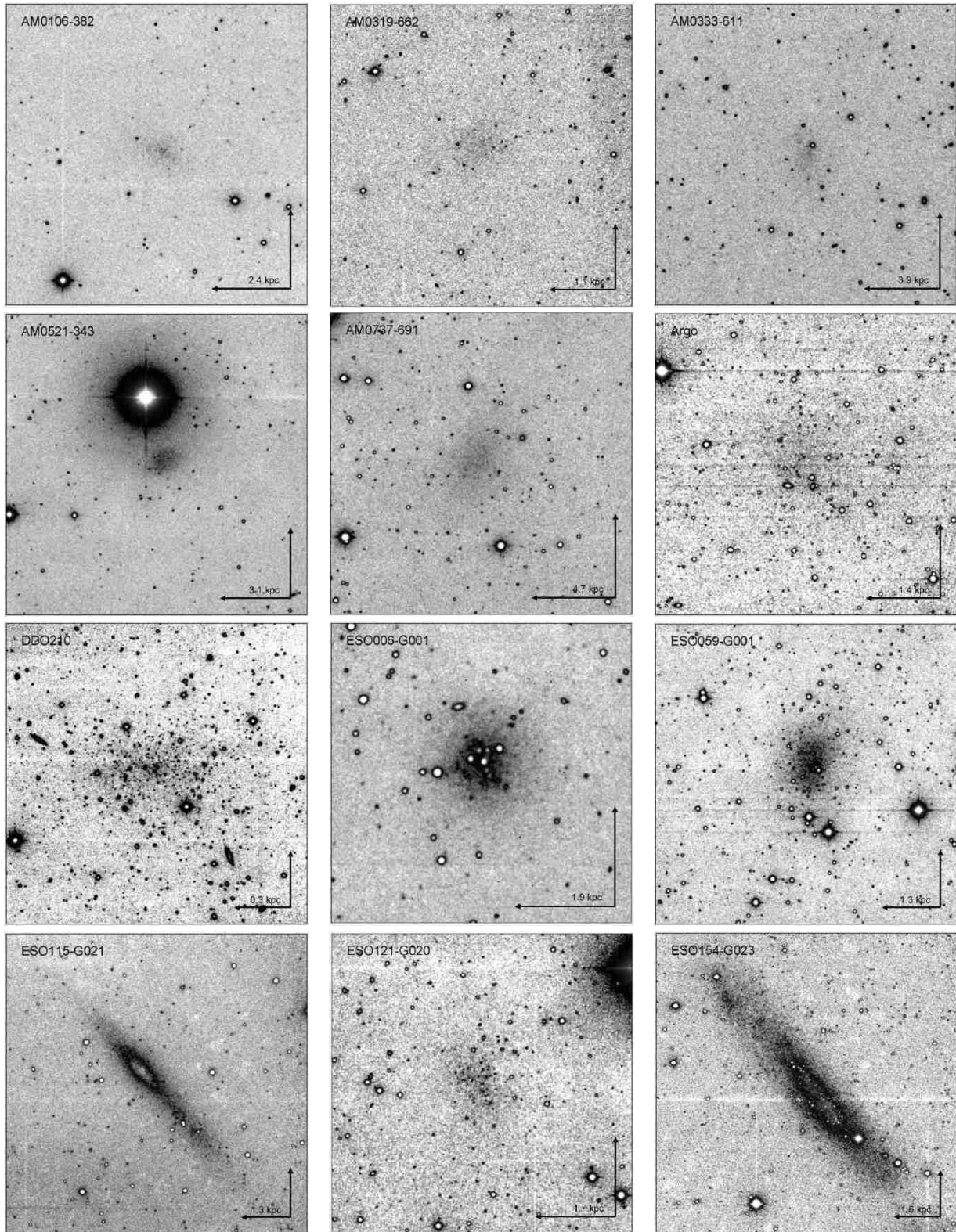


FIG. 2.— LSI deep H -band images from the 3.9m Anglo-Australian Telescope. Here the scale represents 1 arcmin. The corresponding linear scale is also indicated. North is up and East is to the left. The intensity is represented by a greyscale which goes from white (low intensity) to black (medium intensity) and then back to white (high intensity). Higher resolution version available at <http://www.mso.anu.edu.au/~emma/KirbyHband.pdf>

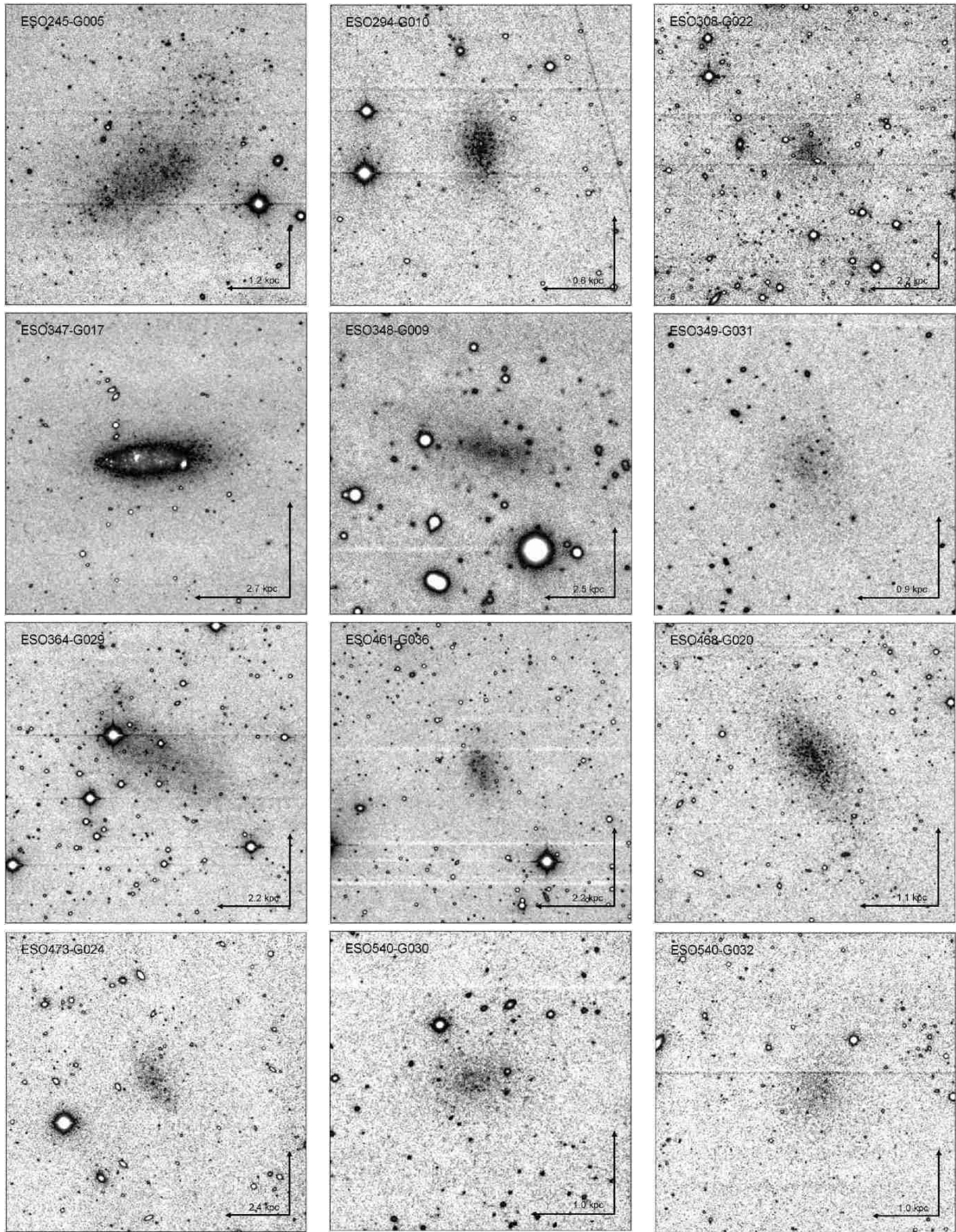


FIG. 3.— LSI deep H -band images from the 3.9m Anglo-Australian Telescope. Here the scale represents 1 arcmin. The corresponding linear scale is also indicated. North is up and East is to the left. The intensity is represented by a greyscale which goes from white (low intensity) to black (medium intensity) and then back to white (high intensity). Higher resolution version available at <http://www.mso.anu.edu.au/~emma/KirbyHband.pdf>

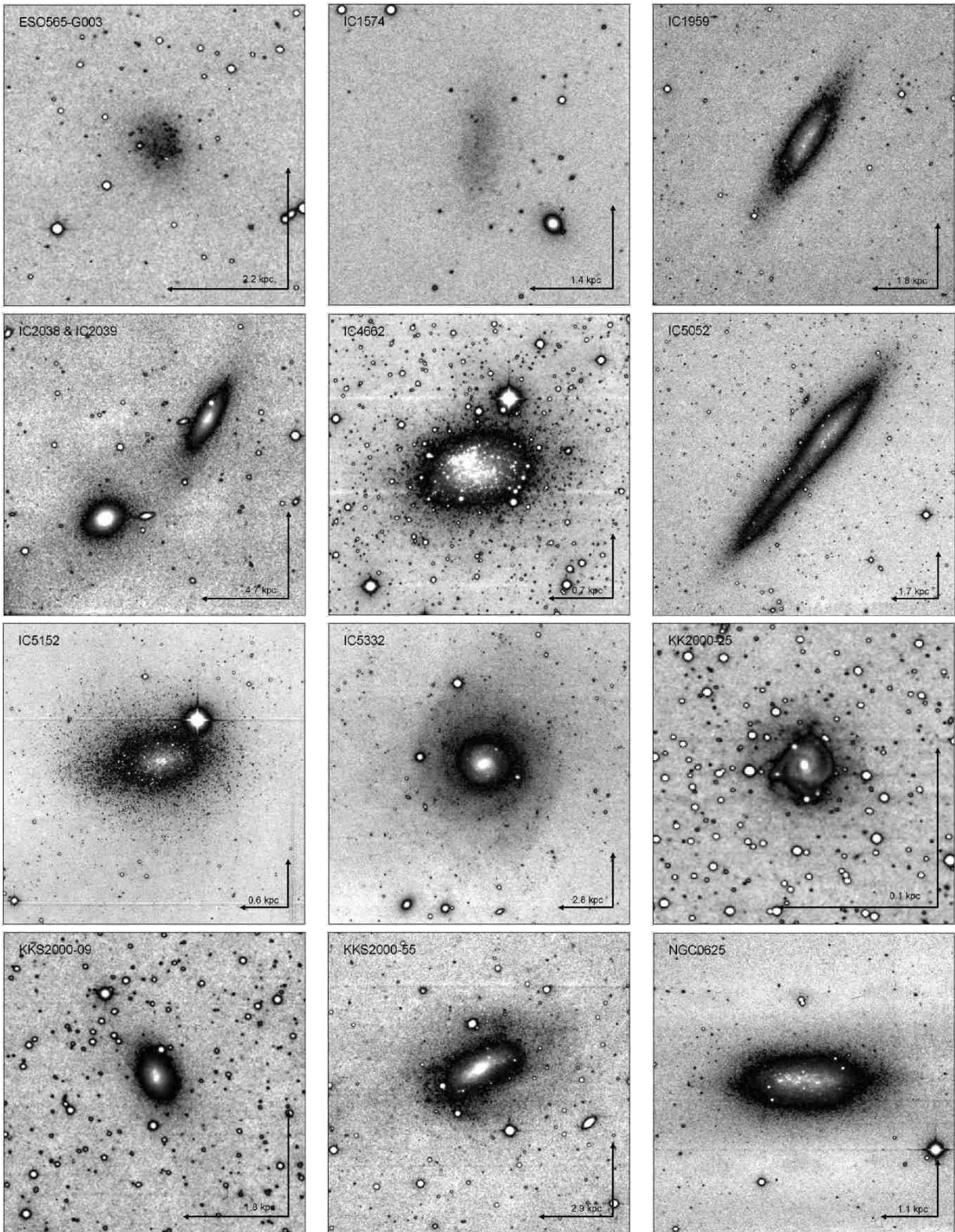


FIG. 4.— LSI deep H -band images from the 3.9m Anglo-Australian Telescope. Here the scale represents 1 arcmin. The corresponding linear scale is also indicated. North is up and East is to the left. The intensity is represented by a greyscale which goes from white (low intensity) to black (medium intensity) and then back to white (high intensity). Higher resolution version available at <http://www.mso.anu.edu.au/~emma/KirbyHband.pdf>

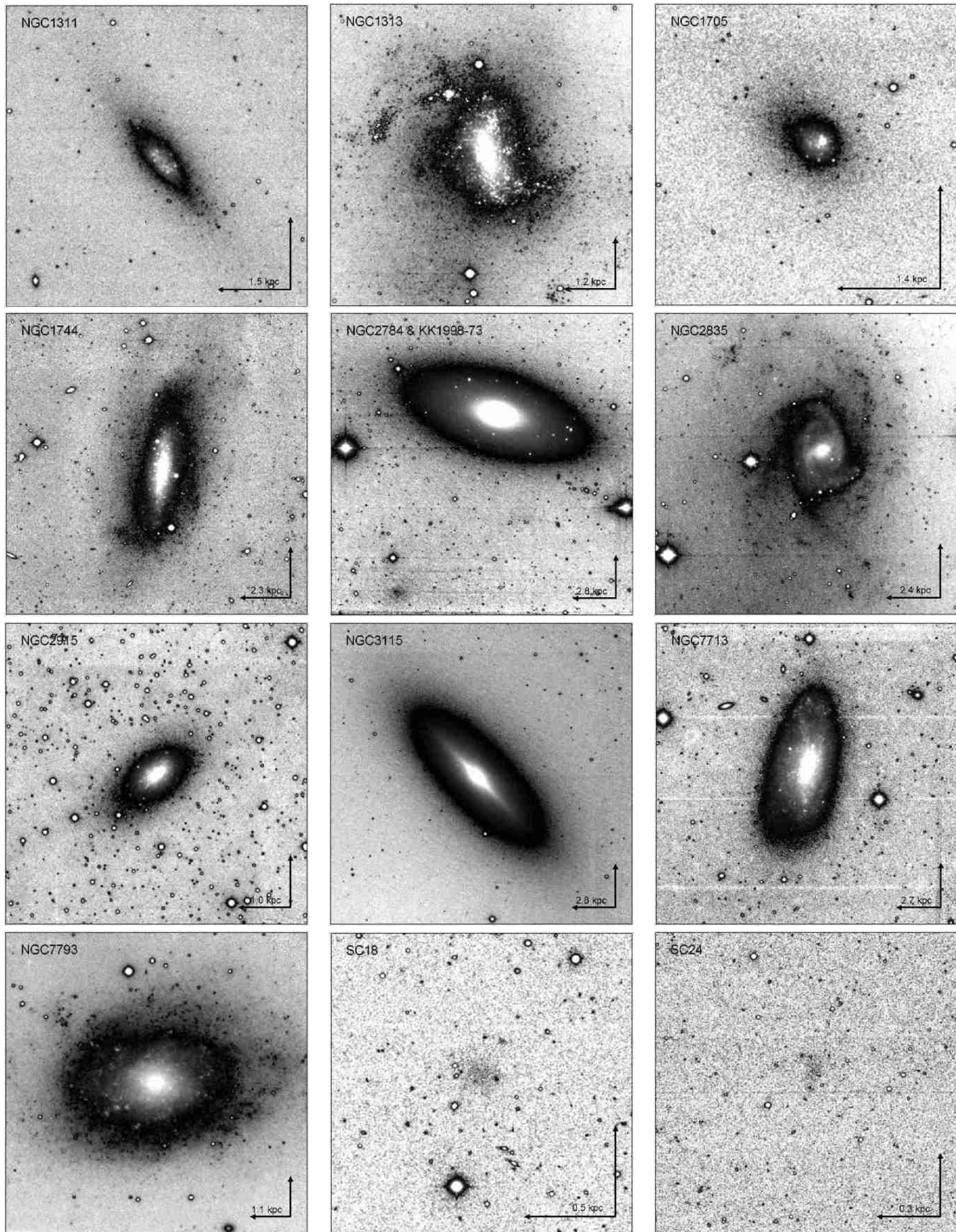


FIG. 5.— LSI deep H -band images from the 3.9m Anglo-Australian Telescope. Here the scale represents 1 arcmin. The corresponding linear scale is also indicated. North is up and East is to the left. The intensity is represented by a greyscale which goes from white (low intensity) to black (medium intensity) and then back to white (high intensity). Higher resolution version available at <http://www.mso.anu.edu.au/~emma/KirbyHband.pdf>

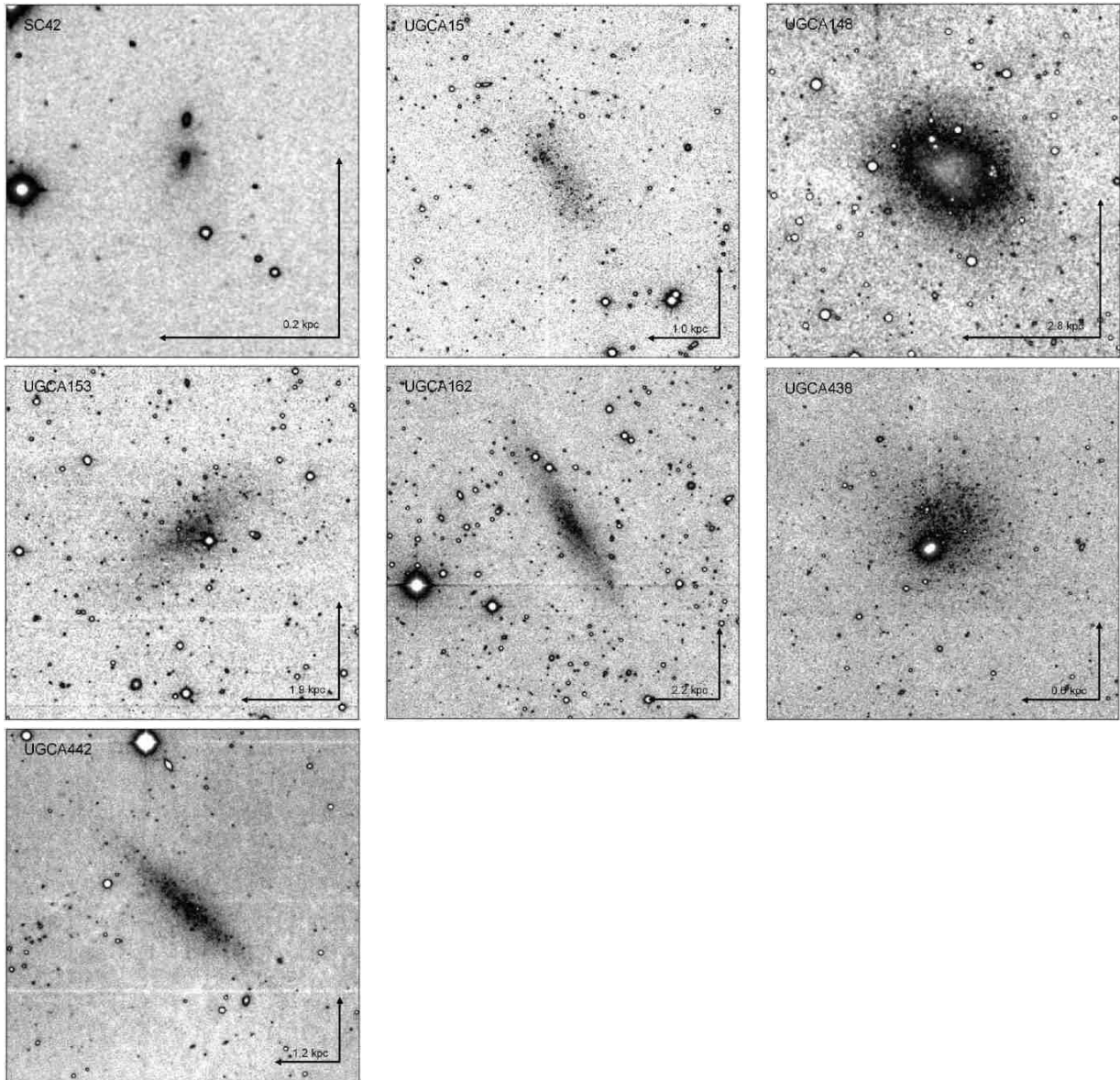


FIG. 6.— LSI deep H -band images from the 3.9m Anglo-Australian Telescope. Here the scale represents 1 arcmin. The corresponding linear scale is also indicated. North is up and East is to the left. The intensity is represented by a greyscale which goes from white (low intensity) to black (medium intensity) and then back to white (high intensity). Higher resolution version available at <http://www.mso.anu.edu.au/~emma/KirbyHband.pdf>

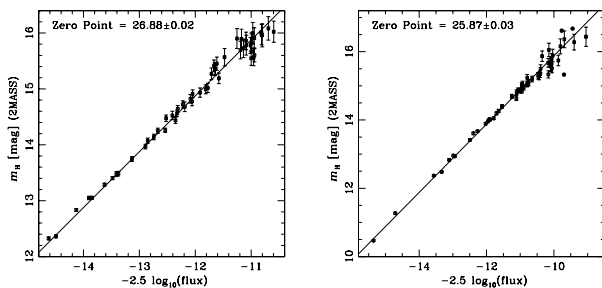


FIG. 7.— Instrumental versus 2MASS H -band magnitudes for foreground stars around the galaxies ESO121-G020 (left) and UGCA153 (right). Both galaxies were observed for the same amount of time and the difference of one mag in zero-point is due to the presence of thin clouds when UGCA153 was observed.

calculated with IRAF's ELLIPSE package as a function

of radius. The ellipticity and position angle were, in general, settled in the outer regions of the galaxies, however, in some cases they varied significantly in the inner regions.

Table 3 lists the measured properties of the 57 sample galaxies: column (1) galaxy name, (2) observed integrated apparent magnitude, $m_{H,obs}$, (3) effective radius, r_{eff} , (4) mean effective surface brightness, $\langle\mu_H\rangle_{eff}$, (5) ellipticity and (6), position angle of the major axis measured in degrees from North through East (PA= 90°). The listed ellipticity and position angle is that of the outermost isophote fitted.

The surface brightness profile for each galaxy was fitted with the Sérsic function, $\mu(r) = \mu_0 + 1.086(r/\alpha)^n$ (or $I(r) = I_0 \exp(-(r/\alpha)^n)$), using IRAF's NFIT1D procedure. Extrapolation of the surface brightness profile to infinity with the help of the Sérsic function allows us

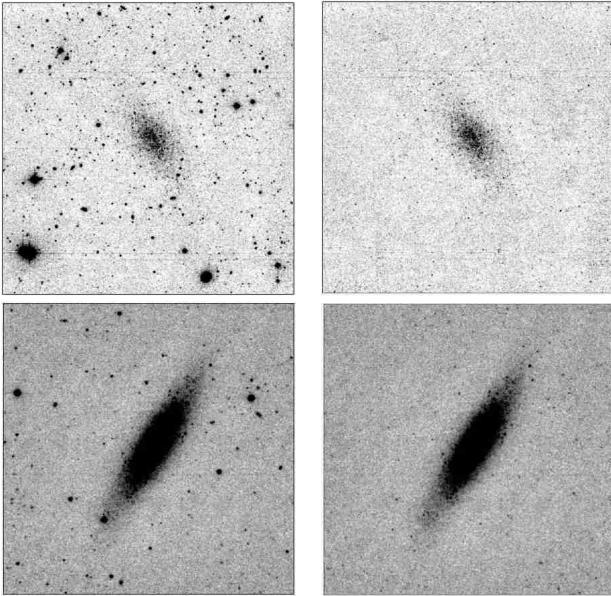


FIG. 8.— Two examples of the effectiveness of the foreground cleaning process. Shown are the before and after cleaning images of ESO468-G020 [upper panel] and IC1959 [lower panel]. Higher resolution version available at <http://www.mso.anu.edu.au/~emma/KirbyHband.pdf>

to make an accurate estimate of the amount of flux that remained undetected in the sky background noise. Using the Sérsic parameter, n , the scale length, α , and the central surface brightness, μ_0 , we calculated the magnitude of the galaxy between the maximum radius and the limit $r = \infty$:

$$\begin{aligned} \Delta m &= -2.5 \log_{10}(I_{\text{missing}}/I_{\text{tot}}) \\ &= -2.5 \log_{10}(\Gamma[2/n, (r_{\text{max}}/\alpha)^n]/\Gamma[2/n]) \end{aligned}$$

where:

$$\begin{aligned} I_{\text{missing}} &= \int_{r_{\text{max}}}^{\infty} 2\pi I_0 \exp[-(r/\alpha)^n] r dr \\ &= \frac{2\pi I_0 \alpha^2}{n} \Gamma[2/n, (r_{\text{max}}/\alpha)^n] \end{aligned} \quad (1)$$

and

$$\begin{aligned} I_{\text{tot}} &= \int_0^{\infty} 2\pi I_0 \exp[-(r/\alpha)^n] r dr \\ &= \frac{2\pi I_0 \alpha^2}{n} \Gamma[2/n]. \end{aligned} \quad (2)$$

Thereby $\Gamma(a, x)$ is the upper incomplete gamma function and r_{max} was taken to be the radius at which the growth curve reaches within 5% of the asymptotic intensity. The missing flux introduces a systematic error to the total magnitude $m_{H, \text{obs}}$. This correction Δm was typically less than 0.2 mag (see Table 4), except in the few cases, e.g. NGC3115, where the galaxy's angular size extends beyond the IRIS2 FoV. We note that those galaxies have been observed in the CSJ mode to estimate the sky level from dedicated blank sky observations. AM0521-343 was not corrected for missing flux as the bright foreground star prevented the fitting of its surface brightness profile.

The corrected total apparent magnitude, $m_H = m_{H, \text{obs}} - \Delta m$, was converted into a luminosity using the

standard equations

$$M_{H,0} = m_H - 5 \log_{10} D - 25 - A_H$$

and

$$L = 10^{0.4(M_{H,\odot} - M_{H,0})}$$

where $M_{H,\odot} = 3.35$ mag is the H -band luminosity of the sun (Colina et al. 1996) and $A_H = 0.576 \cdot E(B - V)$ is the Galactic extinction (Schlegel et al. 1998). The accuracy of the reddening-corrected absolute magnitude, $M_{H,0}$, is dominated by the accuracy of the distance.

The effective radius, r_{eff} , is the aperture radius which encloses half the total light of a galaxy. This quantity is systematically underestimated unless corrected for the amount of undetected flux. The corrected effective radius, R_{eff} is defined implicitly by the equation

$$\frac{I_{\text{tot}}}{2} = \frac{2\pi I_0 \alpha^2}{n} \cdot \Gamma\left[\frac{2}{n}, \left(\frac{R_{\text{eff}}}{\alpha}\right)^n\right] \quad (3)$$

where I_0 , α , and n are the Sérsic parameters for a particular galaxy. The solution for all $n \in [0.25, 2]$ can be approximated by the equation

$$R_{\text{eff}} \approx \alpha \left(\frac{2}{n} - 0.33211 \right)^{1/n}. \quad (4)$$

Within the quoted uncertainties, there is no deviation between the approximate analytic solution (equation 4) and the numerical solution of equation 3.

The H -band luminosity of each galaxy was converted into a stellar mass using a mass-to-light ratio of $\Upsilon_*^H = 1.0 \pm 0.4$. This conversion factor is discussed in detail in Section 4.2. The derived parameters are listed in Table 4 for the 57 LSI galaxies: column (1) galaxy name, (2) effective radius, r_{eff} , in kpc, (3), (4) and (5) the Sérsic parameters μ_0 , n and α , (6) the missing flux, Δm , (7) and (8) the corrected effective radius, R_{eff} , in arcsec and kpc, (9) absolute H magnitude, $M_{H,0}$, and (10) the total stellar mass, $\log_{10} \mathcal{M}_*$.

4.1. Galactic extinction correction

The extinction correction used in our study is that of Schlegel et al. (1998). We prefer these IR emission maps over the older Burstein & Heiles (1978, 1982, 1984) models as the reddening is derived directly from dust emission rather than HI column densities and galaxy counts. The Schlegel et al. (1998) maps have a typical uncertainty of 16%. However, for low latitudes, $|b| < 5^\circ$, most contaminating sources were not removed from the maps leading to larger errors for that part of the sky. This difficulty can not be circumvented by using the Burstein & Heiles maps as they do not include latitudes below $|b| < 10^\circ$. Consequently, the reddening corrections applied to the two sample galaxies KK2000-25 and KKS2000-09 are less secure. This uncertainty will particularly affect the quoted B -band magnitudes. The H -band results will be affected to a lesser extent as the correction is of order one-tenth of that in the B -band.

Should one choose to use the Burstein & Heiles models the difference in our results is minimal. There are only two sample galaxies (KKS2000-09 and ESO461-G036) which have significantly different absolute B -band magnitudes. In these two cases we apply an average of the

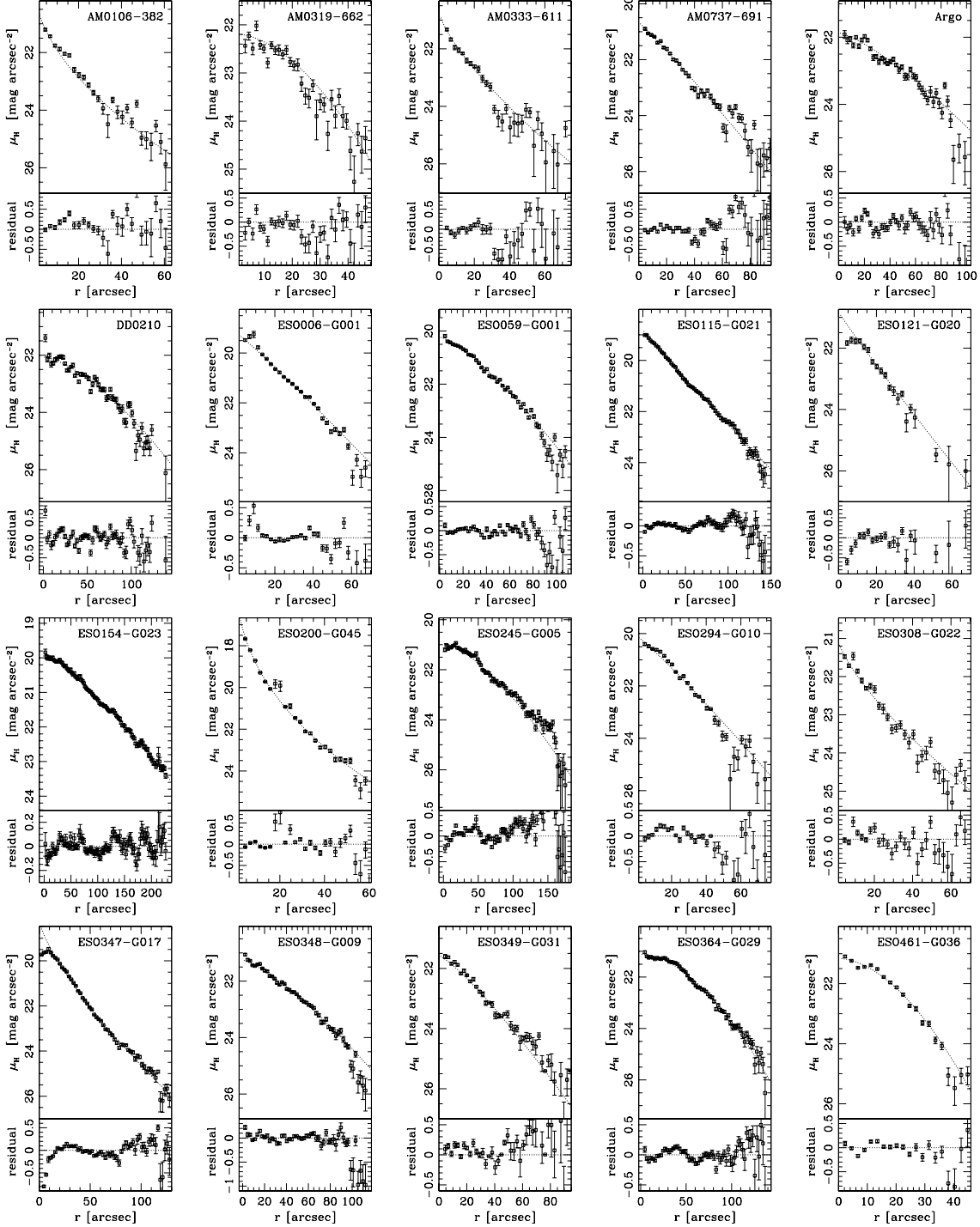


FIG. 9.— H -band surface brightness profiles for all program galaxies except AM0521-343 (see text). The best fitting Sérsic profile is shown as solid line together with the residuals.

Burstein and Heiles and the Schlegel et al. corrections. The choice of the reddening estimate does not change the H -band results within the quoted errors.

4.2. The H -band mass-to-light ratio

For our analysis we will adopt a H -band mass-to-light ratio that is well supported by observations and theory. Assuming a typical 12 Gyr old, solar metallicity, stellar population with a constant star formation rate and a Salpeter initial mass function, the de Jong

(1996) model yields a mass-to-light ratio of $\Upsilon_*^H = 1.0$. This is consistent with the empirically derived value of $\Upsilon_*^H = 0.9 \pm 0.6$ obtained for our sample by using each galaxy's $B - H$ colour (Tables 2 and 3) and adopting the colour-dependent stellar mass-to-light ratio relation from the Bell & de Jong (2001) galaxy evolution models. Finally, these two mass-to-light ratios are well in the range of $0.7 < \Upsilon_*^H < 1.3$ which is based on observed SDSS colours $0.1 < (g - r) < 1.1$ for 22,679 galaxies and 2MASS photometry (Bell et al. 2003). From these three

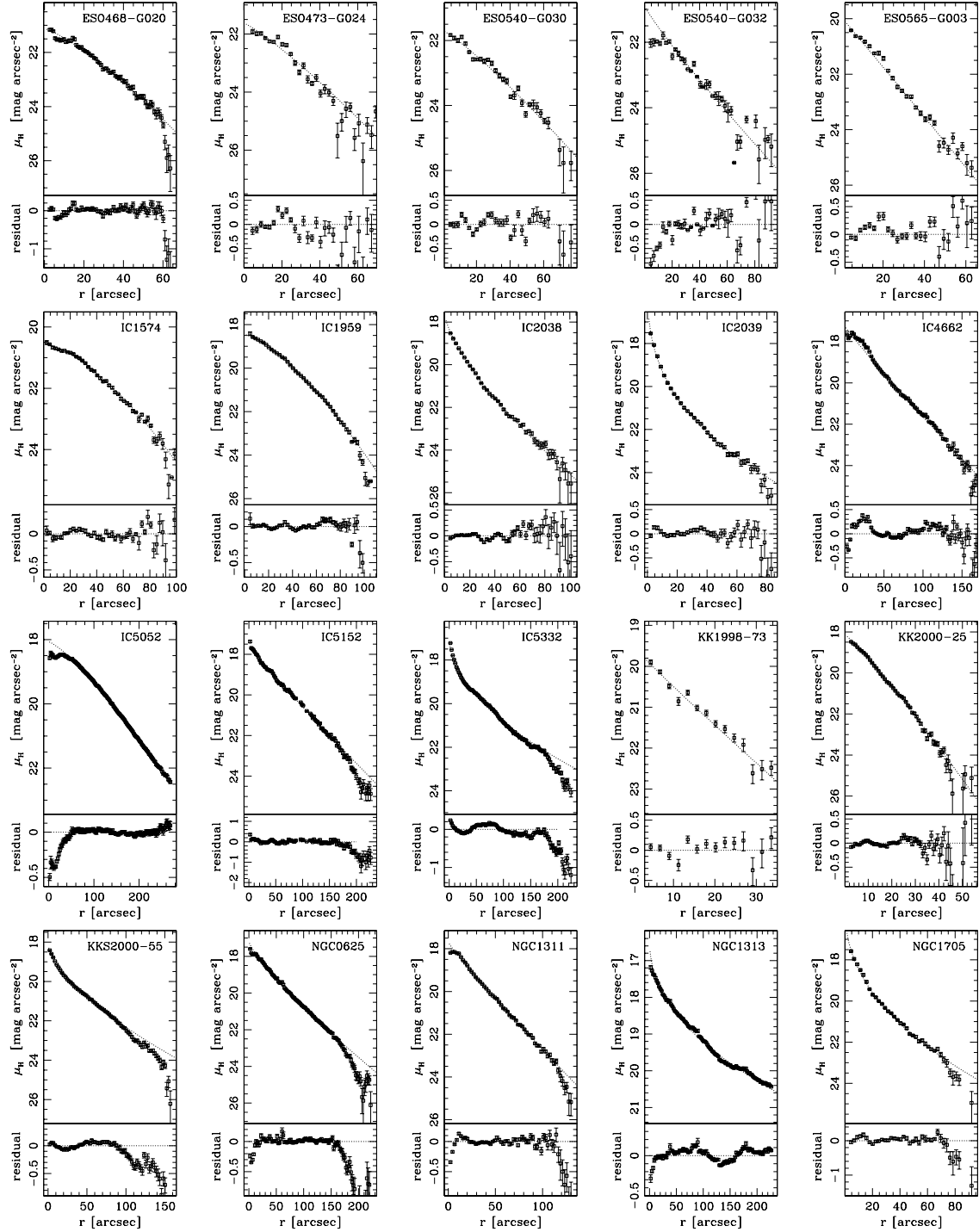


FIG. 10.— H -band surface brightness profiles for all program galaxies except AM0521-343 (see text). The best fitting Sérsic profile is shown as solid line together with the residuals.

independent values we derive the error weighted mean of $\Upsilon_*^H = 1.0 \pm 0.4$.

5. ARE THERE ANY GENUINE YOUNG GALAXIES?

Observations for 11 galaxies were not included in our photometric study either because the galaxy remained invisible in the final mosaics despite our faint H -band surface brightness limit of $24 - 26 \text{ mag arcsec}^{-2}$, or the galaxy was detected but foreground stars interfered with the analysis. In this section, we discuss the four galaxies

labelled as “no galaxy detected” in Table 1: AM0717-571, KK2000-04, KK2000-06 and NGC2784 DW1. While they remain as candidates for galaxies with a pure young stellar component, we show it is unlikely that this is the case. We also include KK2000-03 which had a marginal detection, and the galaxy pair HIZOAJ1616-55 and SJK98 J1616-55 which were not detected but we note that the images had serious foreground contamination.

A lower bound of the total apparent magnitude for

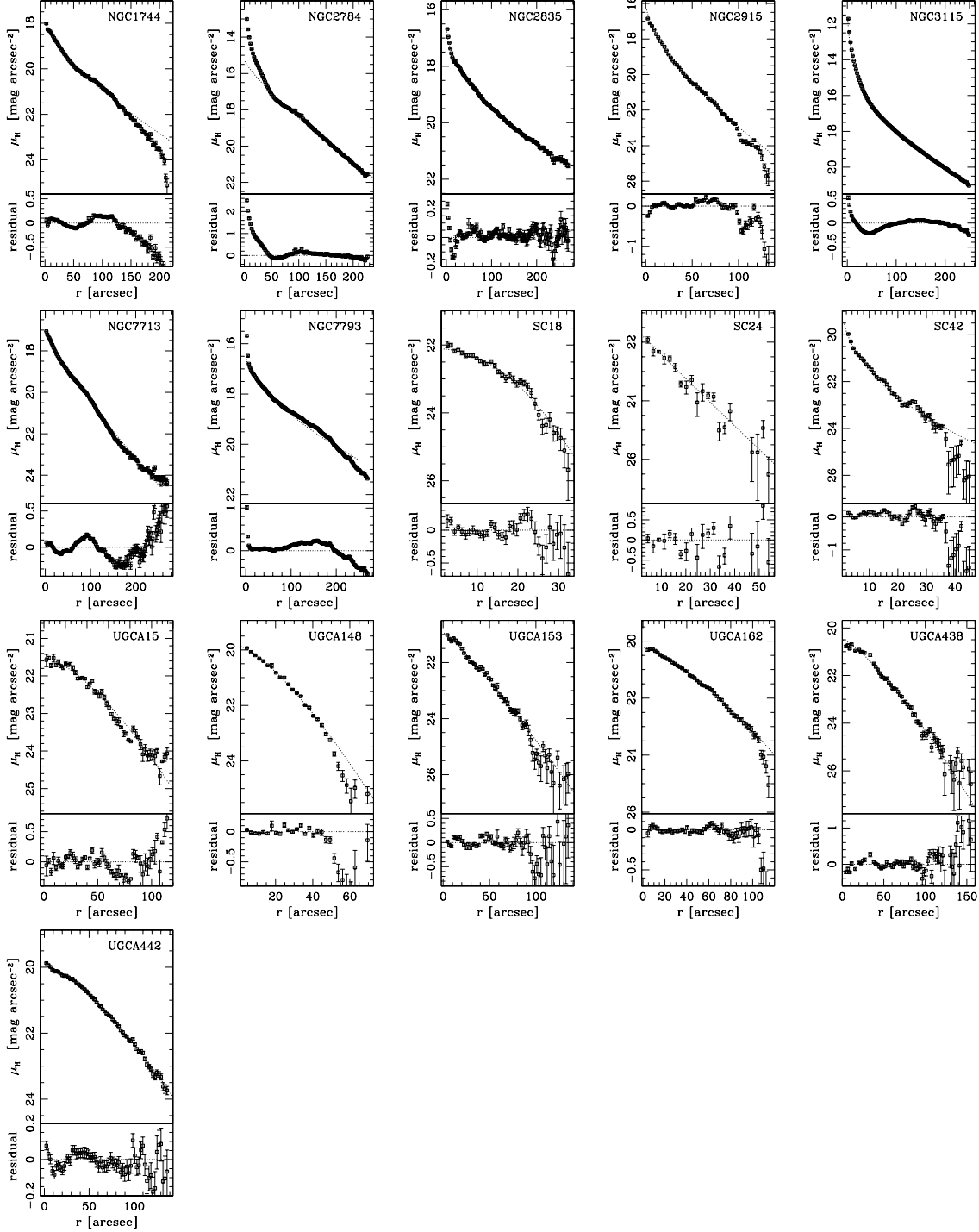


FIG. 11.— H -band surface brightness profiles for all program galaxies except AM0521-343 (see text). The best fitting Sérsic profile is shown as solid line together with the residuals.

these galaxies can be calculated. For that purpose, we consider a hypothetical galaxy with a constant star density equivalent to the survey's mean surface brightness limit of $\langle \mu_{0,lim} \rangle = 25 \text{ mag arcsec}^{-2}$ out to a cutoff radius, r_{cut} , at which point the stellar density drops to zero. We set the cutoff radius, r_{cut} , to be 250 arcsec which is equivalent to the size of the largest galaxies in our sample. This yields the brightest apparent magni-

tude an undetected galaxy could possibly have:

$$m_{tot} > \mu_{0,lim} - 2.5 \log_{10}(\pi r_{cut}^2) = 11.8 \text{ mag}. \quad (5)$$

This lower bound is applicable to AM0717-571, KK2000-04, KK2000-06 and NGC2784 DW1 but not KK2000-03 which has a foreground star located directly in front of the galaxy (see discussion below), nor HIZOAJ1616-55 and SJK98 J1616-55 which have serious foreground contamination. A lower bound on the absolute magnitude and an upper bound on the stellar mass is calculated

TABLE 1
GALAXIES NOT ANALYSED FURTHER.

Name (1)	R.A. (J2000.0) (2)	Decl. (J2000.0) (3)	Reason (4)	m_H (mag) (5)	$M_{H,0}$ (mag) (6)	$\log_{10}(\mathcal{M}_*)$ $\log_{10}(\mathcal{M}_*)$ (7)
KK2000-03	02:24:44.58	-73:30:49.2	marginal detection	—	—	—
KK2000-04	03:12:46.14	-66:16:12.5	no galaxy detected	> 11.8	> -16.5	< 7.0
KK2000-06	03:14:26.14	-66:23:27.9	no galaxy detected	> 11.8	> -16.5	< 7.9
ESO490-G017	06:37:57.09	-26:00:03.1	foreground stars	—	—	—
HIZSS003	07:00:29.3	-04:12:30	foreground stars	—	—	—
ESO558-PN011	07:06:56.80	-22:02:26.0	foreground stars	—	—	—
AM0717-571	07:18:37.90	-57:24:46.5	no galaxy detected	> 11.8	> -18.7	< 8.8
NGC2784 DW1	09:12:18.5	-24:12:41	no galaxy detected	> 11.8	> -18.3	< 8.7
SJK98 J1616-55	16:16:49.0	-55:44:57	Galactic plane	—	—	—
HIZOAJ1616-55	16:18:46	-55:37:30	Galactic plane	—	—	—
ESO594-G004	19:29:58.97	-17:40:41.3	foreground stars	—	—	—

using distances from the literature (see Table 1).

AM0717-571

Although AM0717-571 has appeared in several lists of nearby galaxies (eg. Karachentseva & Karachentsev 1998; Whiting et al. 2002, 2007), this object was actually never followed-up in the optical or near-IR and consequently was never confirmed to be a galaxy. The only optical (B -band) image available comes from the Digital Sky Survey (DSS) and shows an object with a morphology resembling closely that of a Galactic nebula. An HI signal at the position of AM0717-571 was reported by HIPASS and included in the HIPASS Bright Galaxy Catalog (Koribalski et al. 2004). However, to understand this apparent detection one has to know that AM0717-571 has two neighboring galaxies, ESO123-G001 and ESO162-G017, located at an angular distance of only 20.7 and 22.4 arcmin respectively. These two galaxies have heliocentric velocities of 1160 km s^{-1} and 1098 km s^{-1} similar to and bracketing AM0717-571's listed velocity of 1148 km s^{-1} . The HIPASS spectra at the RA, DEC positions of ESO162-G017 and AM0717-571 are almost identical in velocity width and peak flux. The fact that our deep H -band image did not reveal any galaxy and considering the relatively large uncertainty of HIPASS coordinates due to the 15 arcmin beam size of the Parkes Radio Telescope, it is conceivable that the 21cm emission at 1148 km s^{-1} detected by HIPASS is coming from the extended HI halos of ESO162-G017 and/or ESO123-G001. It has been pointed out by Koribalski et al. (2004) that larger offsets between the HI and the optical positions usually occur when multiple galaxies contribute to the signal or when the HI distribution is asymmetric or peculiar. A clarification of the true nature of AM0717-571 will require further investigations.

HIZOAJ1616-55 AND SJK98 J1616-55

HIZOAJ1616-55 (Juraszek et al. 2000; listed as HIZOAJ1618-55 in NED) and SJK98 J1616-55 have almost identical catalog positions and are close to the Galactic plane ($b = -3.8^\circ$). Staveley-Smith et al. (1998) concluded from deep ATCA 21 cm mapping that these objects are likely part of a single or interacting pair of low-mass HI galaxies with a total HI mass of $8 \times 10^7 \mathcal{M}_\odot$. Their heliocentric velocities (402 km s^{-1} and 430 km s^{-1}) are very similar to that of the Circinus

galaxy (439 km s^{-1} ; Jones et al. 1998) suggesting a possible physical connection to Circinus and the nearby Cen A group. However, no optical counterparts have been found to date and hence it is plausible that the HI detection originates from a compact high velocity cloud (Putman et al. 2002). To search for more evidence for either scenario we included HIZOAJ1616-55 and SJK98 J1616-55 in our imaging survey. The Galactic extinction in the H -band ($A_H = 0.4 \text{ mag}$) is much lower than in the optical (eg. $A_B = 2.7 \text{ mag}$) and hence increases the chances to detect the stellar components of these objects at low Galactic latitude. However, despite our deep imaging, no stellar counterpart to the HI was found and consequently the picture of high velocity cloud(s) seems more plausible.

KK2000-03

KK2000-03, also known as PGC 9140, is well away from the Galactic plane at $l = 294.2$, $b = -42.0$ but remained almost invisible on our 1800 sec H -band image. Whiting et al. (2007) list the galaxy and report an R -band surface brightness of $23.7 \pm 0.2 \text{ mag arcsec}^{-2}$. They calculate this as the average surface brightness for an area of roughly 1 arcmin in diameter, located such that it contains the brightest parts of the galaxy, and excludes stars (where possible). Assuming an $R - H$ color of 1.10 for the sun (calculated using results from Colina et al. 1996) implies KK2000-03 should have an H -band surface brightness of $22.6 \text{ mag arcsec}^{-2}$, well above our detection limit. The DSS image shows that KK2000-03 is located directly behind a foreground star. Despite this contamination, KK2000-03 must have an unusual blue stellar population for it not to be detected more prominently in our survey.

KK2000-04 AND KK2000-06

Little is known about these two extremely low surface brightness irregular galaxies which were first mentioned in a catalogue of dwarf galaxy candidates by Karachentseva & Karachentsev (2000). The authors estimated their total B -band magnitudes from photographic plates as 17.8 and 17.0, respectively, and speculated that they may be companions of the barred spiral NGC 1313 ($v_\odot = 475 \text{ km s}^{-1}$), another of our sample galaxies. We did not detect either KK2000-04 or KK2000-06 despite obtaining deep imaging data of fields with only low levels of

foreground contamination. While KK2000-04 also remains undetected at 21 cm, the H I spectrum for KK2000-06 measured with the Effelsberg 100-m radio telescope (Huchtmeier et al. 2001) suggests a heliocentric velocity of $\sim 2250 \text{ km s}^{-1}$. Therefore it is possible that KK2000-04 is a plate flaw and KK2000-06 is a distant galaxy unrelated to NGC1313.

NGC2784 DW1

The extremely low surface brightness dwarf galaxy NGC2784 DW1 was first detected by Parodi et al. (2002). It is located between the S0 galaxy NGC2784 and the nucleated early-type dwarf KK98-73 on the sky and due to its morphology (dE), its size and location, Parodi et al. (2002) suggest it is likely to be a satellite of NGC2784. Karachentsev et al. (2004) give NGC2784 DW1 a membership distance and include it in the census of galaxies within 10 Mpc. However, it is important to note that no independent distance measurement has been obtained to date. Our deep near-IR observation detected the faint galaxy KK98-73, while NGC2784 DW1 is barely visible as expected from the recorded mean effective surface brightness of $\langle \mu \rangle_{eff} \approx 25 \text{ mag arcsec}^{-2}$ and $r_{eff} \approx 20 \text{ arcsec}$ in the B -band.

6. RESULTS

6.1. LSI survey versus 2MASS photometry

It is instructive to see how galaxies can change their appearance when going from 2MASS to the deeper LSI observations. For example, our image of the barred Sc galaxy NGC2835 (Fig. 12) reveals the rich near-IR morphology and extent of this spiral galaxy for the first time. The almost face-on view presents a well-ordered 4 or 5-arm spiral pattern outlined by the star-dominated Population II disk, which closely traces the gas-dominated Population I disk morphology observed in the B -band (Sandage & Bedke 1994). The 2MASS image for the irregular Sculptor group galaxy ESO473-G024 shows qualitatively the limitation of that survey to study dwarf galaxies. With a central H -band surface brightness of $\approx 20.5 \text{ mag arcsec}^{-2}$, ESO473-G024 remains effectively undetected in 2MASS (Fig. 12). Our image uncovers a smooth, dE-like morphology with little evidence of irregularity. This stands in stark contrast to the B -band image that is dominated by a number of prominent H II regions and dust features.

It has been previously pointed out by Andreon (2002) that the short integration time of 2MASS failed to detect most of the lower surface brightness (dwarf) galaxies and that, if they were detected, fluxes were underestimated by as much as 70 percent. To investigate this issue further, we plot in Figure 13 the difference between our total extrapolated apparent magnitudes ($m_{H,obs} - \Delta m$; Table 3, col. 2 and Table 4, col 6) and the total magnitudes from the 2MASS All-Sky Extended Source Catalog for 21 galaxies we have in common, as a function of mean effective surface brightness ($\langle \mu_H \rangle_{eff}$; Table 3, col. 4). LSI galaxies with a surface brightness fainter than $\mu_H = 18 \text{ mag arcsec}^{-2}$ are affected at different levels with the missing flux in the range between 0.2 and 2.5 mag. Even in the cases of the luminous galaxies NGC2784 and NGC3115 our analysis finds that their 2MASS H -band magnitudes are 0.5 mag too faint.

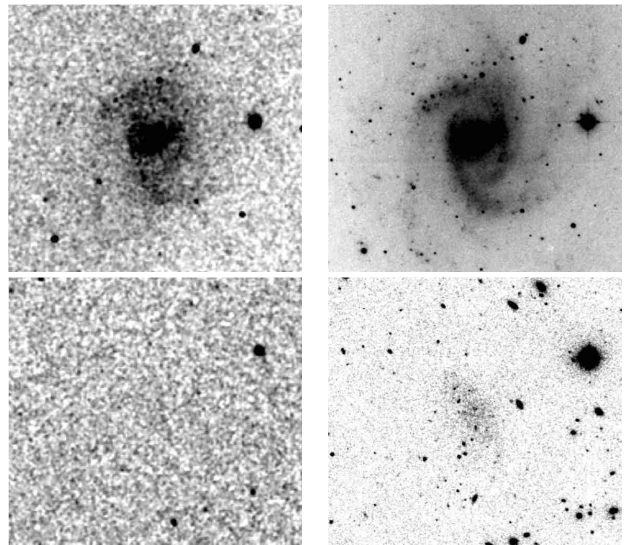


FIG. 12.— The 2MASS (left panel) and the LSI (right panel) H -band images of the spiral galaxy NGC2835 ($V_{helio} = 886 \text{ km s}^{-1}$) and the dwarf irregular galaxy ESO473-G024 ($V_{helio} = 541 \text{ km s}^{-1}$) are shown in the upper and lower panels, respectively. The new LSI images probe to surface brightness levels $\approx 4 \text{ mag arcsec}^{-2}$ fainter than 2MASS. A complex morphology and additional spiral arms are detected in the case of NGC2835 whereas only the deeper LSI image detects a stellar component in the case of ESO473-G024. Higher resolution version available at <http://www.mso.anu.edu.au/~emma/KirbyHband.pdf>

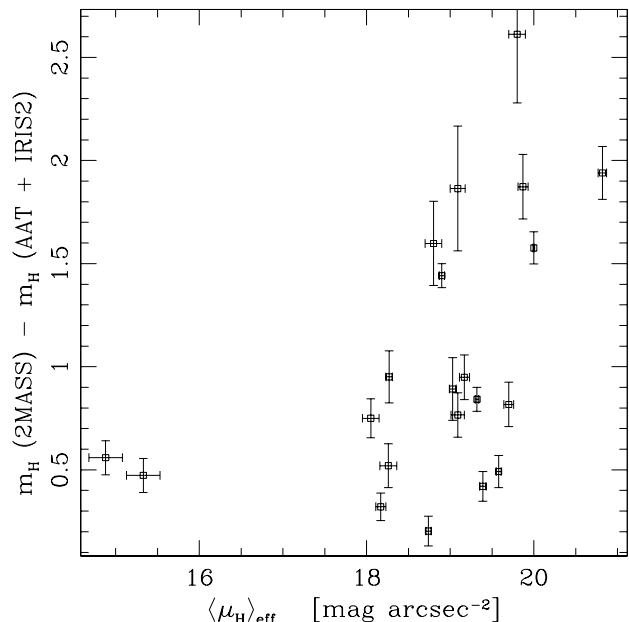


FIG. 13.— 2MASS versus LSI magnitudes showing the systematic underestimation of galaxy fluxes by 2MASS for the galaxies that it did detect.

To demonstrate that the disparity between the 2MASS and our H -band magnitudes is not caused by differences in the measuring procedure we analysed 2MASS images using our method. The photometric parameters listed in the 2MASS Extended Source Catalog, as well as the surface brightness profiles, were reproduced within the quoted uncertainties. It should be noted that the 2MASS Large Galaxy Atlas (Jarrett et al. 2003) has employed

two different methods for recovering the flux below the sky background noise and that we have made the comparison to the magnitudes which were obtained by extrapolating the surface brightness profile. The 2MASS magnitudes which were obtained using Kron (1980) apertures are systematically fainter (see Figure 9 of Jarrett et al. 2003) and therefore the difference between our total apparent magnitudes and the 2MASS magnitudes obtained using Kron apertures is also larger.

The Extended Source Catalog is contaminated by a small (1% to 5%) number of artefacts which can significantly affect the photometry of real sources (Jarrett et al. 2000). Each of our galaxy images were visually inspected for artefacts which were effectively removed (unless documented otherwise). This is obviously an impractical approach for the much larger 2MASS dataset and Jarrett et al. (2000) notes that the pipeline is not 100% effective. It is conceivable that this accounts for a fraction of the discrepancy.

In summary, our finding is in good agreement with that of Andreon (2002) and emphasizes again that the 2MASS magnitudes are significantly fainter than those obtained from deeper near-IR imaging. As the mean effective surface brightness correlates with the luminosity of a galaxy (see §6.3, Figure 17), serious selection biases must be expected, for instance, for the 2MASS-based H -band galaxy luminosity function at magnitudes fainter than $M_H = -20$ mag.

6.2. Optical - Near Infrared magnitude transformation

The $B - H$ colour of each galaxy is an indicator of the ratio of the population II to population I stars, as modulated by the effects of dust. A comparison of the absolute B - and H -band magnitude, corrected for Galactic extinction, is shown in Figure 14 for our sample galaxies. We also plot the Virgo cluster data from the Goldmine database (Gavazzi et al. 2003). The data of the Virgo galaxies were extinction-corrected using $A_B = 0.13$ mag and $A_H = 0.01$ mag. We have adopted the mean cluster distance of 15.8 Mpc (Jerjen et al. 2004) based on surface brightness fluctuation measurements of early-type galaxies. In addition to the Virgo cluster data, we have also included the data for 30 bright spiral galaxies from Kassin et al. (2006) which were corrected for extinction (using Schlegel et al. 1998). By including the two additional data sets we are able to investigate the $B - H$ colour for late-type galaxies over a range of 15 magnitudes. Figure 14 shows that there is a tight correlation between the B - and H -band luminosity of a galaxy. This linear relation is

$$M_{H,0} = (1.14 \pm 0.02)M_{B,0} - (0.74 \pm 0.32) \quad (6)$$

which is a least squares fit to the Virgo cluster data. While the more luminous galaxies in our sample obey the relation closely, the residual plot suggests that the scatter marginally increases in the dwarf regime and possibly has a slight upwards trend to redder colours (average residual ≈ 1 mag). The most deviant galaxy in our sample, KK2000-25, appears under-luminous in the B -band by 3 magnitudes. While we cannot exclude the possibility that this galaxy has had an unusual star formation history, we need to point out two things. Firstly, KK2000-25 is located almost in the Galactic plane ($b = 1.28^\circ$) and

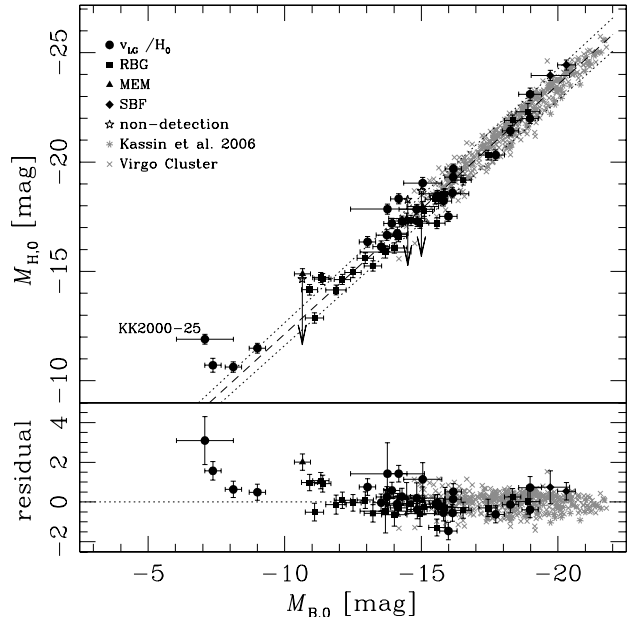


FIG. 14.— Comparison of the integrated absolute B - and H -band magnitude. Plotted here is our new data with an indicator of the distance estimate method. Also plotted is the data of Kassin et al. (2006) and the Virgo cluster data from the Goldmine database (Gavazzi et al. 2003). Marked is the galaxy KK2000-25 which appears to be significantly under-luminous in the B -band. The dashed line is the $B - H$ mean colour for all galaxies in the Virgo Cluster sample and the dotted lines indicates data within 1σ . The galaxies which were not detected have been given a lower bound magnitude estimate.

thus has a large B -band extinction uncertainty. Secondly, the B -band magnitude for KK2000-25 was estimated visually from a photographic film (Huchtmeier et al. 2001). Consequently, the deviation from the line of best fit could be entirely due to a large uncertainty in the B -band magnitude. By excluding KK2000-25, there is no correlation between the residual in the $B - H$ plot and the galaxy distance, Galactic latitude or mean effective surface brightness (see Figure 15).

It is worth noticing that the least squares fit deviates from a line of unity slope. The gradient of 1.14 ± 0.02 implies that dwarf galaxies are in general bluer than the more luminous galaxies. It is well known that galaxy colour correlates with luminosity (eg, Tully et al. 1998; Hogg et al. 2002; Blanton et al. 2001, 2003).

Figure 14 gives a useful indication of the stellar population of galaxies. Galaxies which lie well below the line are bluer than most galaxies which suggests that they have a relatively young stellar population. Conversely, galaxies which lie well above the line are redder than expected indicating a larger old stellar population. The tight correlation (correlation coefficient = 0.97) between the B - and H -band luminosities comes somewhat as a surprise. A B -band light profile of a galaxy can be significantly attenuated and distorted by dust. Moreover, short-lived giant O and B stars contribute to the B -band emission and hence the profile can be distorted by transient star-formation events. The stellar mass of most galaxies is dominated by the older, low luminosity stellar population whose energy output peaks at near-IR wavelengths (Gavazzi et al. 1996b). Hence it has been ar-

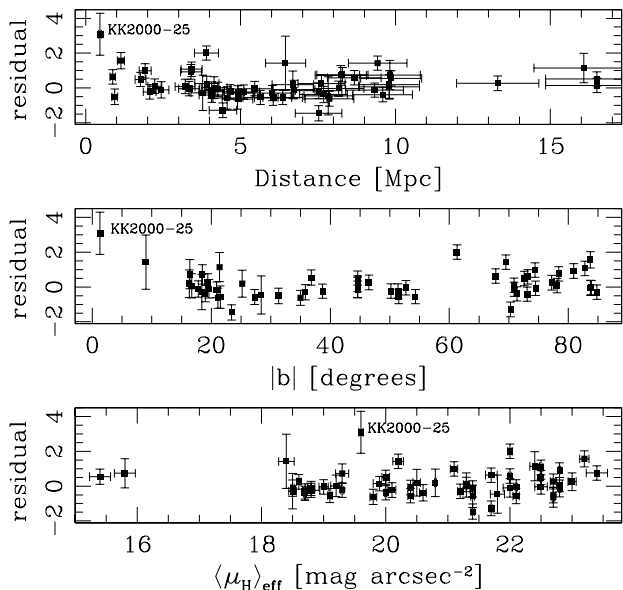


FIG. 15.— The deviation of individual LSI galaxies from equation 6 as a function of distance [upper panel], Galactic latitude [middle panel] and mean effective surface brightness [lower panel]. The error in the distance is taken to be 10%. KK2000-25 is located at low Galactic latitude and significantly deviates from the relationship.

gued that the near-IR is the optimal wavelength regime for investigations of structural properties (Driver 2004). The tight correlation between the B - and H -bands, however, suggests that the advantages of the H -band may not be as significant as previously thought, at least for late-type giant galaxies. A detailed comparison of the observed scatter with the predictions from population synthesis models (eg, Bruzual & Charlot 1993, 2003; Maraston 1998; Li & Han 2008) is beyond the scope of this paper because of the wide range of stellar compositions and star formation histories represented by our galaxy sample.

The $B - H$ colour for each galaxy can be compared with the morphological type (Figure 16). There we include the combined samples of Kassin et al. (2006) and the Virgo cluster data in the white boxes and the new LSI data is shown by the black boxes. The combined Virgo cluster and Kassin et al. (2006) sample is ten times the size of our sample but is dominated by giant, luminous galaxies. Our sample, in contrast, contains four times as many irregular dwarf galaxies. Therefore, when interpreting the color vs morphology plot, it must be noted that our sample dominates the morphological bin of irregular galaxies and the literature data dominates the larger galaxies.

The comparison of morphology to the $B - H$ colour shows that the early-type galaxies are redder than the late-type, irregular and dwarf galaxies. A similar study by Jarrett et al. (2003) for galaxies in the 2MASS Large Galaxy Atlas also showed this trend.

6.3. Luminosity - Surface Brightness Relation

In Figure 17 we plot the mean effective surface brightness of our sample galaxies as a function of absolute magnitude. In addition to our H -band data, we include 560

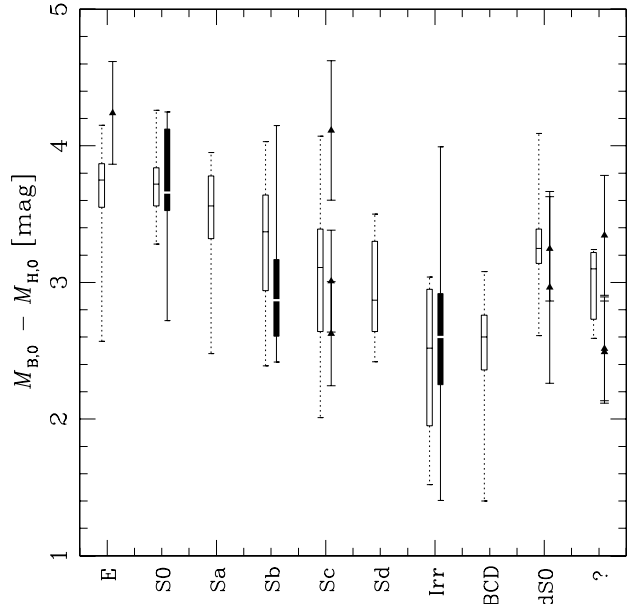


FIG. 16.— Comparison of the integrated apparent $B - H$ colour and the morphological type. The black boxes show our data and the white boxes show the combined samples of Kassin et al. (2006) and the Virgo cluster data listed in the Goldmine database (Gavazzi et al. 2003). The boxes show the median values as well as the quartile range. The errorbars on the boxes show the maximum and minimum $B - H$ colour for each morphological type. For morphologies with insufficient data, the individual data points are displayed with their associated uncertainty.

late-type Virgo cluster galaxies (obtained from the Goldmine database; Gavazzi et al. 2003). The mean effective surface brightness for Virgo cluster galaxies was calculated as

$$\langle \mu_H \rangle_{eff} = M_H + 2.5 \log_{10}(\pi r_{eff}^2)$$

and the data was corrected for extinction using $A_H = 0.01$ mag. The morphologies of Virgo cluster galaxies included in the sample range from S0 to Sd, Irr and BCD (listed as types 1 to 18 in the Goldmine database).

As previously discussed in de Jong & Lacey (2000), the relationship between the two photometric parameters provides an important link to the underlying physical parameters of a galaxy, namely its total mass \mathcal{M}_{tot} and total angular momentum. The total angular momentum of a galaxy, expressed as the dimensionless spin parameter $\lambda = J|E|^{1/2}\mathcal{M}_{tot}^{-5/2}G^{-1}$ (Peebles 1969), is related to the scale length of its disk (Fall & Efstathiou 1980; Dalcanton et al. 1997; Mao et al. 1998). de Jong & Lacey (2000) showed that λ can be transformed into observable quantities. The authors presented a model of a singular isothermal sphere with $E \propto \mathcal{M}_{tot}V_c^2$ from the virial theorem and a perfect exponential disk with angular momentum $J_{disk} \propto \mathcal{M}_{disk}r_{eff}V_c$ (assuming $V_{disk} = V_c$). They showed that if $J_{disk}/\mathcal{M}_{disk} \propto J/\mathcal{M}_{tot}$ and $\mathcal{M}_{disk} \propto \mathcal{M}_{tot}$ then $\lambda \propto r_{eff}V_c^2/\mathcal{M}_{disk}$. Furthermore, using the relation $\mathcal{M}_{tot} \propto V_c^3$ predicted for dark matter halos, de Jong and Lacey showed that $\lambda \propto r_{eff}L^{\Upsilon/3}$, where Υ is the mass-to-light ratio for the disk. This can be transformed into an expression between surface

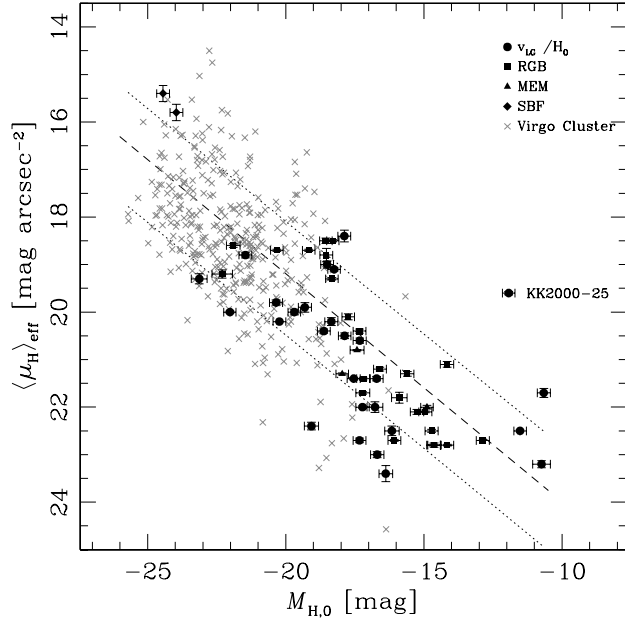


FIG. 17.— Comparison of the mean effective surface brightness and the absolute magnitude for our sample galaxies. Symbol shapes indicate the distance estimation method used. Also plotted are 560 late-type galaxies in the Virgo cluster (Gavazzi et al. 2003). Marked is the galaxy KK2000-25 which deviates from the general trend probably caused by an incorrect distance estimate. The dashed line is the line of best fit for all galaxies and the dotted lines indicates data within 1σ .

brightness and total magnitude by invoking

$$\Sigma_{eff} = L(2\pi r_{eff}^2)^{-1}$$

which results in:

$$\lambda \propto \Sigma_{eff}^{-1/2} L^{-\Upsilon/3+1/2}$$

Using the two identities $-2.5 \log_{10} \Sigma_{eff} = \langle \mu_H \rangle_{eff} + c$ and $-2.5 \log_{10} L = M + c'$ (c and c' being constants) we finally arrive at the theoretical luminosity – surface brightness relation:

$$\langle \mu \rangle_{eff} = (1 - 2\Upsilon/3)M + 5 \log_{10} \lambda + C \quad (7)$$

Here, we can see that the gradient of the luminosity – surface brightness relation is a function of the galaxy mass-to-light ratio and that the dispersion in the empirical relation reflects the distribution of the spin parameter.

The empirical relation between the two observational quantities in Figure 17 for the late-type galaxies of the Virgo cluster sample is analytically best described by the linear equation:

$$\langle \mu_H \rangle_{eff} = a \cdot M_{H,0} + b \quad (8)$$

where a is 0.47 ± 0.08 , 0.44 ± 0.06 and 0.48 ± 0.05 for our LSI sample, the Virgo cluster sample and the combined LSI + Virgo samples respectively, and b is 29.0 ± 1.4 , 28.0 ± 1.3 and 28.8 ± 1.1 . The uncertainty in a and b is the formal uncertainty in the linear fit plus the uncertainty due to the robustness of the sample obtained using bootstrap resampling. In Figure 17, the empirical relation between the mean effective surface brightness and the absolute magnitude is plotted for the combined LSI + Virgo cluster samples.

A comparison of the empirical result (see equation 8) with the theoretical prediction (equation 7) allows to estimate Υ_*^H : $a = (1 - 2\Upsilon/3) \Rightarrow \Upsilon_*^H = 0.80 \pm 0.12$, 0.84 ± 0.09 and 0.78 ± 0.08 for our LSI sample, the Virgo cluster sample and the combined data sets respectively. These results are in excellent agreement with the value of 1.0 ± 0.4 adopted in section 4.2.

7. INTERESTING GALAXIES

KK2000-09

KK2000-09 has a morphological classification of a spiral “S”. However, close inspection of our H -band image reveals that KK2000-09 has a double nucleus and thus should be classified as a peculiar galaxy.

HIZSS003

HIZSS003 is a HI source originally detected at 21 cm by the Dwingeloo obscured galaxies survey (Henning et al. 1998). It is located behind the zone of avoidance ($b = 0.09^\circ$) in the outskirts of the LG at 1.7 Mpc (Silva et al. 2005). Our image is highly contaminated with foreground stars preventing further analysis. Begum et al. (2005) show that HIZSS003 is actually a galaxy pair (HIZSS003A and HIZSS003B). Our imaging shows that there is a resolved stellar overdensity associated with the HI peak (labelled HIZSS003A using the Begum et al. 2005 convention) as well as a stellar component associated with the peak of the narrowband H_α emission first detected by Massey et al. (2003) (labelled HIZSS003B by Begum et al. 2005).

KK2000-25

The morphology of KK2000-25 is listed in NED as Irr. Our deep imaging (see Figure 4, third row, right panel) shows distinct spiral arms and that KK2000-25 should have a morphological classification of “Sb”. This morphology is not consistent with its angular size given the listed distance of 0.5 Mpc. This distance estimate was obtained using a HI profile observed by Huchtmeier et al. (2001) and the spectrum given does not show a clear galaxy detection. Based on the updated morphological classification, KK2000-25 must be more distant than the estimate given.

The galaxy KK2000-25, although prominent when observed in the H -band, appears to be under-luminous in the B -band (see Figure 14). This galaxy, however, is located at a low Galactic latitude and hence the extinction correction will not be very reliable. An inaccurate extinction correction will affect the B -band magnitude significantly but will have minimal affect on the H -band magnitude. Hence it is possible that this galaxy does not obey the H -band to B -band transformation (equation 6) simply because the absolute B -band magnitude is incorrect. The discrepancy between the absolute B - and H -band for KK2000-25 is not due to the incorrect distance estimate.

8. SUMMARY

We have presented the deepest H -band images available to date for 57 galaxies in the Local Sphere of Influence ($D < 10$ Mpc), obtained using the near-IR camera IRIS2 at the 3.9m Anglo-Australian Telescope. Of the 68 targets, 11 remained undetected or could not be

usefully analysed due to contamination by foreground stars. The surface brightness limit reaches down to $\mu_{lim} < 26$ mag arcsec, 4 magnitudes fainter than 2MASS.

The images, cleaned from Galactic foreground contamination, reveal the morphology and extent of many of the galaxies for the first time. For 56 galaxies, we derive radial luminosity profiles, ellipticities, and position angles, together with global parameters such as total magnitude, mean effective surface brightness, half-light radius, Sérsic parameters, and stellar mass.

No genuine young galaxies have been found in this survey. Some sample galaxies were previously identified on *B*-band photographic plates but remain undetected in the near-IR. In each case there is a plausible alternative explanation for the non-detection:

- AM0717-571: DSS *B_J*-band morphology resembles that of a Galactic nebula, but true nature still remains unclear.
- HIZOAJ1616-55 and SJK98 J1616-55: possibly one or two high velocity clouds.
- KK2000-03: Superimposed star hampers analysis however the marginal detection in the H-band suggests an unusual blue galaxy.
- KK2000-04: Originally assumed to be a companion of NGC1313 however possibly a photographic plate flaw.
- KK2000-06: Originally assumed to be a companion of NGC1313. More likely a background galaxy at ≈ 2250 km s⁻¹.
- NGC2784 DW1: intrinsic extreme low surface brightness dwarf satellite of NGC2784.

We also detected a double nucleus in KKS2000-09 and propose to reclassify this system as a peculiar galaxy. KKS2000-25 was shown to have distinct spiral arms in the *H*-band and thus should be classified as “Sb”. Morphology and angular size strongly suggest that this is a background galaxy beyond 10 Mpc.

We found compelling evidence that the short integration time of 2MASS resulted in serious underestimation of a galaxy’s luminosity. The magnitudes of

galaxies, with *H*-band surface brightnesses fainter than 18 mag arcsec⁻², obtained in our study are up to 2.5 mag brighter than those obtained by 2MASS. As the mean effective surface brightness correlates with the luminosity of a galaxy, we expect serious selection biases for a 2MASS-based *H*-band galaxy luminosity function fainter than $M_H = -20$ mag.

There is a tight correlation (correlation coefficient = 0.97) between the *B*- and *H*-band magnitudes of a galaxy and this correlation has been demonstrated over a range of 15 magnitudes. The linear transformation between the *B*- and *H*-bands has a small scatter (0.3 mag) for bright galaxies. In the dwarf regime, there is a marginal increase in scatter and possibly a slight trend for galaxies to be redder (by approximately 1 magnitude) than indicated by the transformation found for bright galaxies.

The galaxy luminosity – mean effective surface brightness relation has been analysed to derive a semi-empirical stellar mass-to-light ratio of $\Upsilon_*^H = 0.78 \pm 0.08$ in the *H*-band.

All raw and reduced *H*-band images of the 57 program galaxies in this near-IR survey will be made publicly available and can be obtained via email request.

9. ACKNOWLEDGMENTS

We thank the referee for the useful comments. The authors acknowledge financial support from the Australian Research Council Discovery Project Grant DP0451426. This paper is based on data obtained with the Anglo-Australian Telescope. The study made use of data products from the Two Micron All Sky Survey (2MASS), which is a joint project of the University of Massachusetts and the Infrared Processing and Analysis Center/California Institute of Technology, funded by the National Aeronautics and Space Administration and the National Science Foundation. Support for IRIS2 data reduction within ORAC-DR is provided by the Joint Astronomy Centre. This research has made use of the GOLD Mine Database. This research has made use of the NASA/IPAC Extragalactic Database (NED) which is operated by the Jet Propulsion Laboratory, California Institute of Technology, under contract with the National Aeronautics and Space Administration. This research has made use of NASA’s Astrophysics Data System.

REFERENCES

- Aloisi, A., Clementini, G., Tosi, M., et al. 2007, ApJ, 667, L151
Aloisi, A., van der Marel, R. P., Mack, J., et al. 2005, ApJ, 631, L45
Andreon, S. 2002, A&A, 382, 495
Barnes, D. G., Staveley-Smith, L., de Blok, W. J. G., et al. 2001, MNRAS, 322, 486
Begum, A., Chengalur, J. N., Karachentsev, I. D., & Sharina, M. E. 2005, MNRAS, 359, L53
Bell, E. F. & de Jong, R. S. 2001, ApJ, 550, 212
Bell, E. F., McIntosh, D. H., Katz, N., & Weinberg, M. D. 2003, ApJS, 149, 289
Blanton, M. R., Dalcanton, J., Eisenstein, D., et al. 2001, AJ, 121, 2358
Blanton, M. R., Hogg, D. W., Bahcall, N. A., et al. 2003, ApJ, 594, 186
Boselli, A., Gavazzi, G., Franzetti, P., Pierini, D., & Scodreggio, M. 2000, A&AS, 142, 73
Bruzual, G. & Charlot, S. 1993, ApJ, 405, 538
Bruzual, G. & Charlot, S. 2003, MNRAS, 344, 1000
Burstein, D. & Heiles, C. 1978, ApJ, 225, 40
Burstein, D. & Heiles, C. 1982, AJ, 87, 1165
Burstein, D. & Heiles, C. 1984, ApJS, 54, 33
Carrasco, E. R., Mendes de Oliveira, C., Infante, L., & Bolte, M. 2001, AJ, 121, 148
Colina, L., Bohlin, R. C., & Castelli, F. 1996, AJ, 112, 307
Corbin, M. R., Kim, H., Jansen, R. A., Windhorst, R. A., & Fernandes, R. C. 2008, ApJ, 675, 194
Côté, S., Freeman, K. C., Carignan, C., & Quinn, P. J. 1997, AJ, 114, 1313
Dalcanton, J. J., Spergel, D. N., & Summers, F. J. 1997, ApJ, 482, 659
de Jong, R. S. 1996, A&A, 313, 377
de Jong, R. S. & Lacey, C. 2000, ApJ, 545, 781
Driver, S. 2004, Publications of the Astronomical Society of Australia, 21, 344
Driver, S. P., Popescu, C. C., Tuffs, R. J., et al. 2007, MNRAS, 379, 1022
Fall, S. M. & Efstathiou, G. 1980, MNRAS, 193, 189

- Gavazzi, G., Boselli, A., Donati, A., Franzetti, P., & Scodreggio, M. 2003, *A&A*, 400, 451
- Gavazzi, G., Franzetti, P., Scodreggio, M., et al. 2000, *A&AS*, 142, 65
- Gavazzi, G., Pierini, D., Baffa, C., et al. 1996a, *A&AS*, 120, 521
- Gavazzi, G., Pierini, D., & Boselli, A. 1996b, *A&A*, 312, 397
- Gavazzi, G., Pierini, D., Boselli, A., & Tuffs, R. 1996c, *A&AS*, 120, 489
- Henning, P. A., Kraan-Korteweg, R. C., Rivers, A. J., et al. 1998, *AJ*, 115, 584
- Hogg, D. W., Blanton, M., Strateva, I., et al. 2002, *AJ*, 124, 646
- Hubble, E. P. 1936, Yale University Press
- Huchtmeier, W. K., Karachentsev, I. D., & Karachentseva, V. E. 2001, *A&A*, 377, 801
- Jarrett, T. H., Chester, T., Cutri, R., et al. 2000, *AJ*, 119, 2498
- Jarrett, T. H., Chester, T., Cutri, R., Schneider, S. E., & Huchra, J. P. 2003, *AJ*, 125, 525
- Jerjen, H., Binggeli, B., & Barazza, F. D. 2004, *AJ*, 127, 771
- Jerjen, H., Binggeli, B., & Freeman, K. C. 2000, *AJ*, 119, 593
- Jerjen, H., Freeman, K. C., & Binggeli, B. 1998, *AJ*, 116, 2873
- Jerjen, H., Rekola, R., Takalo, L., Coleman, M., & Valtonen, M. 2001, *A&A*, 380, 90
- Juraszek, S. J., Staveley-Smith, L., Kraan-Korteweg, R. C., et al. 2000, *AJ*, 119, 1627
- Karachentsev, I. D., Dolphin, A., Tully, R. B., et al. 2006, *AJ*, 131, 1361
- Karachentsev, I. D., Karachentseva, V. E., Huchtmeier, W. K., & Makarov, D. I. 2004, *AJ*, 127, 2031
- Karachentsev, I. D., Karachentseva, V. E., Suchkov, A. A., & Grebel, E. K. 2000, *A&AS*, 145, 415
- Karachentseva, V. E. & Karachentsev, I. D. 1998, *A&AS*, 127, 409
- Karachentseva, V. E. & Karachentsev, I. D. 2000, *A&AS*, 146, 359
- Kassin, S. A., de Jong, R. S., & Pogge, R. W. 2006, *ApJS*, 162, 80
- Koribalski, B. S. 2007, in *Galaxies in the Local Volume*, ed. B. S. Koribalski & H. Jerjen
- Koribalski, B. S., Staveley-Smith, L., Kilborn, V. A., et al. 2004, *AJ*, 128, 16
- Kraan-Korteweg, R. C. & Tammann, G. A. 1979, *Astronomische Nachrichten*, 300, 181
- Kron, R. G. 1980, *ApJS*, 43, 305
- Lauberts, A. & Valentijn, E. A. 1989, *The surface photometry catalogue of the ESO-Uppsala galaxies* (Garching: European Southern Observatory, —c1989)
- Li, Z. & Han, Z. 2008, *MNRAS*, 387, 105
- Maddox, S. J., Efstathiou, G., Sutherland, W. J., & Loveday, J. 1990, *MNRAS*, 243, 692
- Makarova, L. N., Karachentsev, I. D., Grebel, E. K., et al. 2005, *A&A*, 433, 751
- Mao, S., Mo, H. J., & White, S. D. M. 1998, *MNRAS*, 297, L71
- Maraston, C. 1998, *MNRAS*, 300, 872
- Massey, P., Henning, P. A., & Kraan-Korteweg, R. C. 2003, *AJ*, 126, 2362
- Parodi, B. R., Barazza, F. D., & Binggeli, B. 2002, *A&A*, 388, 29
- Peebles, P. J. E. 1969, *ApJ*, 155, 393
- Putman, M. E., de Heij, V., Staveley-Smith, L., et al. 2002, *AJ*, 123, 873
- Ryder, S. 2007, *Anglo-Australian Observatory Epping Newsletter*, 111, 25
- Sandage, A. 1961, *The Hubble atlas of galaxies* (Washington: Carnegie Institution, 1961)
- Sandage, A. & Bedke, J. 1994, *The Carnegie atlas of galaxies* (Washington, DC: Carnegie Institution of Washington with The Flintridge Foundation, —c1994)
- Sandage, A. & Binggeli, B. 1984, *AJ*, 89, 919
- Schlegel, D. J., Finkbeiner, D. P., & Davis, M. 1998, *ApJ*, 500, 525
- Schmidt, K.-H. & Boller, T. 1992, *Astronomische Nachrichten*, 313, 329
- Schulte-Ladbeck, R. E., Crone, M. M., & Hopp, U. 1998, *ApJ*, 493, L23+
- Schulte-Ladbeck, R. E., Hopp, U., Greggio, L., & Crone, M. M. 2000, *AJ*, 120, 1713
- Schulte-Ladbeck, R. E., Hopp, U., Greggio, L., Crone, M. M., & Drozdovsky, I. O. 2001, *AJ*, 121, 3007
- Seth, A. C., Dalcanton, J. J., & de Jong, R. S. 2005, *AJ*, 129, 1331
- Silva, D. R., Massey, P., DeGioia-Eastwood, K., & Henning, P. A. 2005, *ApJ*, 623, 148
- Skrutskie, M. F., Cutri, R. M., Stiening, R., et al. 2006, *AJ*, 131, 1163
- Spergel, D. N., Bean, R., Doré, O., et al. 2007, *ApJS*, 170, 377
- Thuan, T. X. & Izotov, Y. I. 1997, *ApJ*, 489, 623
- Tinney, C. G. et al. 2004, *Ground-based Instrumentation for Astronomy*, ed. Moorwood, A. F. M., Masanori, I. (Proceedings of the SPIE)
- Tonry, J. L., Dressler, A., Blakeslee, J. P., et al. 2001, *ApJ*, 546, 681
- Tully, R. B., Pierce, M. J., Huang, J.-S., et al. 1998, *AJ*, 115, 2264
- Vader, J. P. & Chaboyer, B. 1994, *AJ*, 108, 1209
- Vaduvescu, O. & McCall, M. L. 2004, *PASP*, 116, 640
- Whiting, A. B., Hau, G. K. T., & Irwin, M. 2002, *ApJS*, 141, 123
- Whiting, A. B., Hau, G. K. T., Irwin, M., & Verdugo, M. 2007, *AJ*, 133, 715

TABLE 2
BASIC PROPERTIES OF SAMPLE GALAXIES AND OBSERVING LOG

Name (1)	Type (2)	R.A. (J2000.0) (3)	Decl. (J2000.0) (4)	v_{\odot} (km s^{-1}) (5)	v_{LG} (km s^{-1}) (6)	D (Mpc) (7)	Method (8)	m_B (mag) (9)	$E(B-V)$ (mag) (10)	Obs date YYYY-MM-DD (11)	Method (12)	t_{tot} (sec) (13)	Seeing (arcsec) (14)
SC18	LSB	00:00:59.12	-41:09:19.6	151	129	1.8	H	17.30 _j	0.013	2004-10-22	JSF	1620	1.2
ESO349-G031	Irr	00:08:13.36	-34:34:42.0	207	216	3.21	TRGB ^b	15.48 ^a	0.012	2005-01-11	JSF	1620	1.5
ESO294-G010	dS0	00:26:33.37	-41:51:19.0	—	—	1.92	TRGB ^a	15.53 ^a	0.006	2006-01-02	JSF	1620	1.3
ESO473-G024	Irr	00:31:22.51	-22:45:57.5	541	596	8.2	H	16.11 ^e	0.019	2004-10-23	JSF	1620	1.3
SC24	LSB	00:36:38.31	-32:34:25.2	79	83	1.1	H	17.98 _j	0.015	2006-01-02	JSF	1620	1.3
IC1574	Irr	00:43:03.82	-22:14:48.7	363	413	4.92	TRGB ^a	14.36 ^a	0.015	2005-01-11	JSF	1350	1.9
ESO540-G030	Irr	00:49:20.96	-18:04:31.5	—	—	3.4	TRGB ^a	16.37 ^a	0.023	2005-01-10	JSF	1728	1.6
UGCA15	Irr	00:49:49.20	-21:00:54.0	294	346	3.34	TRGB ^a	15.19 ^a	0.017	2004-10-22	JSF	1620	1.3
ESO540-G032	Irr	00:50:24.32	-19:54:24.2	—	—	3.42	TRGB ^a	16.44 ^a	0.020	2006-01-02	JSF	1620	1.4
AM0106-382	dIrr	01:08:21.93	-38:12:34.5	645	605	8.3	H	16.61 ^f	0.012	2004-10-22	JSF	1350	1.1
NGC0625	Sb	01:35:04.63	-41:26:10.3	396	309	4.07	TRGB ^a	11.59 ^a	0.016	2006-01-02	JSF	1620	1.3
SC42	LSB	01:39:15.92	-47:17:51.4	162	64	0.9	H	16.66 _j	0.015	2004-10-22	JSF	1620	1.1
ESO245-G005	Irr	01:45:03.74	-43:35:52.9	394	308	4.43	TRGB ^a	12.73 ^a	0.016	2005-12-29	JSF	1350	1.4
KK2000-03**	dE	02:24:44.58	-73:30:49.20	—	—	4.1	MEM ^a	16.0 ^a	0.051	2006-01-01	JSF	1620	1.9
ESO115-G021	Sc	02:37:48.10	-61:20:18.0	513	337	4.66	TRGB ^a	13.34 ^a	0.026	2005-12-29	JSF	1350	1.4
ESO154-G023	Sb	02:56:50.38	-54:34:17.1	578	412	5.6	H	12.69 ^a	0.017	2004-10-23	CSJ	1800	1.1
KK2000-04**	Irr	03:12:46.14	-66:16:12.5	—	—	4.2***	MEM ⁱ	17.8 ⁱ	0.032	2006-01-01	JSF	810	1.8
KK2000-06**	Irr	03:14:26.14	-66:23:27.9	—	—	4.2***	MEM ⁱ	17.0 ⁱ	0.055	2006-01-01	JSF	810	1.8
NGC1313	Sd	03:18:16.05	-66:29:53.7	475	270	4.15	TRGB ^a	9.66 ^a	0.109	2005-12-30	CSJ	750	1.4
NGC1311	Sb	03:20:06.96	-52:11:07.9	570	398	5.5	H	13.18 ^a	0.021	2005-12-30	JSF	540	1.5
AM0319-662	dIrr	03:21:02.40	-66:19:09.0	232	26	4.07	TRGB ^a	16.5 ^a	0.077	2005-12-30	JSF	810	1.3
IC1959	Sb	03:33:12.59	-50:24:51.3	639	464	6.4	H	13.26 ^a	0.011	2005-12-31	JSF	1620	1.3
AM0333-611	Irr	03:34:15.34	-61:05:47.6	1172	971	13.3	H	16.47 _j	0.032	2004-10-24	JSF	1080	1.2
IC2038	Sd	04:08:53.75	-55:59:22.4	712	505	16.5	MEM ^d	14.98 ^a	0.011	2005-12-31	JSF	1620	1.3
IC2039	S0	04:09:02.37	-56:00:42.1	857	649	16.5	MEM ^d	14.97 ^e	0.012	2005-12-31	JSF	1620	1.3
NGC1705	S0	04:54:13.50	-53:21:39.8	627	400	5.1	TRGB ^a	12.76 ^a	0.008	2004-10-21	JSF	1620	1.1
NGC1744	Sb	04:59:57.80	-26:01:20.0	741	574	7.9	H	11.94 ^e	0.041	2006-01-02	JSF	1620	1.2
AM0521-343	dIrr	05:23:23.72	-34:34:29.5	963	756	10.4	H	15.74 ^g	0.028	2004-10-21	JSF	1620	1.1
KK2000-55**	Sb	05:50:17.71	-10:17:51.6	901	736	10.1	H	—	0.827	2005-12-31	JSF	1620	1.4
ESO364-G029	Irr	06:05:45.22	-33:04:51.0	787	549	7.5	H	13.58 ^a	0.044	2005-12-29	JSF	1620	1.2
ESO121-G020	Irr	06:15:54.19	-57:43:31.6	575	311	6.05	TRGB ^b	15.85 ^a	0.040	2004-10-21	JSF	1620	1.1
ESO490-G017	Irr	06:37:57.09	-26:00:03.10	503	264	4.23	TRGB ^b	14.01 ^a	0.078	2004-10-22	JSF	1080	1.3
ESO308-G022	dIrr	06:39:32.70	-40:43:15.0	821	556	7.6	H	16.05 ^a	0.089	2005-12-30	JSF	810	1.2
KK2000-09**	S	06:46:56.63	-17:56:27.2	693	471	6.5	H	17.2 ^a	0.443	2006-01-01	JSF	1620	1.2
HIZSS003	—	07:00:29.3	-04:12:30	280	101	1.4	H	18 ^a	1.032	2005-12-29	JSF	1620	1.4
Argo	dIrr	07:05:18.80	-58:31:13.0	564	284	4.9	TRGB ^a	14.95 ^a	0.119	2005-12-30	JSF	810	1.2
ESO558-PN011	Irr	07:06:56.80	-22:02:26.0	731	489	6.7	H	14.43 ^a	0.372	2004-10-23	JSF	1620	1.2
AM0717-571	Irr	07:18:37.90	-57:24:46.5	1148	865	11.8	H	—	0.165	2006-01-02	JSF	1620	1.2
ESO059-G001	Irr	07:31:18.20	-68:11:16.8	530	255	4.57	TRGB ^b	13.98 ^a	0.147	2005-12-31	JSF	1620	1.3
AM0737-691	Irr	07:37:12.6	-69:20:31	1456	1174	16.1	H	16.82 ^h	0.213	2004-10-24	JSF	1080	1.1
KK2000-25**	Irr	07:56:38.48	-26:15:01.9	241	-34	0.5***	H	17.7 ^a	0.335	2006-01-02	JSF	810	1.0
ESO006-G001	Sb	08:19:22.14	-85:08:35.9	738	488	6.7	H	15.13 ^a	0.193	2006-01-01	JSF	1620	1.8
UGCA148	Irr	09:09:46.54	-23:00:33.0	725	439	9.8	MEM ^a	15.63 ^a	0.167	2006-01-02	JSF	1620	1.1
NGC2784 DW1	dE	09:12:18.5	-24:12:41	—	—	9.8	MEM ^a	17.27 ^a	0.206	2006-01-01	CSJ	900	1.3
NGC2784	S0	09:12:19.50	-24:10:21.4	697	402	9.82	SBF ^k	11.17 ^a	0.214	2006-01-01	CSJ	900	1.3
KK98-73	dE	09:12:29.30	-24:14:28.0	—	—	9.8	MEM ^a	16.35 ^a	0.197	2006-01-01	CSJ	900	1.3
UGCA153	Irr	09:13:12.08	-19:24:31.0	768	491	6.7	H	15.40 ^a	0.088	2006-01-02	JSF	1620	1.1
NGC2835	Sc	09:17:52.91	-22:21:16.8	886	601	8.2	H	11.03 ^e	0.101	2006-01-01	CSJ	600	1.3
UGCA162	Irr	09:21:28.07	-22:30:06.8	846	560	7.7	H	14.87 ^e	0.067	2006-01-01	JSF	1620	1.2
ESO565-G003	Irr	09:23:10.00	-20:10:03.2	829	549	7.5	H	15.53 ^a	0.062	2006-01-02	JSF	1620	1.2
NGC2915	Irr	09:26:11.53	-76:37:34.8	468	192	3.78	TRGB ^a	13.20 ^a	0.275	2005-01-10	JSF	1728	1.5
NGC3115	S0	10:05:13.98	-07:43:06.9	720	478	9.86	SBF ^k	9.86 ^a	0.047	2006-01-01	CSJ	900	1.4

TABLE 2
BASIC PROPERTIES OF SAMPLE GALAXIES AND OBSERVING LOG

SJK98 J1616-55	—	16:16:49.0	-55:44:57	421	247	3.4	H	—	0.633	2006-05-14	JSF	810	1.4
HIZOAJ1616-55*	—	16:18:46	-55:37:30	409	236	3.2	H	—	0.616	2006-05-04	JSF	810	1.5
IC4662	Irr	17:47:08.86	-64:38:30.3	302	153	2.44	TRGB ^b	11.74 ^a	0.070	2006-05-14	JSF	1620	1.3
ESO594-G004	Irr	19:29:58.97	-17:40:41.3	-79	24	1.04	TRGB ^a	14.12 ^a	0.070	2006-05-14	JSF	1620	1.3
ESO461-G036	dIrr	20:03:57.38	-31:40:53.8	427	470	7.83	TRGB ^b	17.06 ^a	0.296	2006-09-01	JSF	1620	1.2
DDO210	Irr	20:46:51.80	-12:50:52.5	-141	3	0.94	TRGB ^a	14.0 ^a	0.051	2006-05-14	JSF	1620	1.3
IC5052	Sb	20:52:01.63	-69:11:35.9	584	445	6.03	TRGB ^c	11.68 ^a	0.051	2006-09-01	CSJ	450	1.1
IC5152	Irr	22:02:41.51	-51:17:47.2	122	69	2.07	TRGB ^a	11.06 ^a	0.025	2006-09-01	CSJ	750	1.2
ESO468-G020	E3	22:40:43.93	-30:48:00.2	—	—	3.9	MEM ^a	17.36 ^a	0.013	2006-09-02	JSF	1620	1.0
UGCA438	Irr	23:26:27.52	-32:23:19.5	62	99	2.23	TRGB ^a	13.86 ^a	0.015	2004-10-21	JSF	1620	1.1
ESO347-G017	Sb	23:26:56.21	-37:20:48.9	692	688	9.4	H	15.77 ^e	0.017	2006-09-02	JSF	1620	1.0
IC5332	Sa	23:34:27.49	-36:06:03.9	701	700	9.6	H	11.00 ^e	0.017	2006-09-01	CSJ	900	1.3
NGC7713	Sb	23:36:14.99	-37:56:17.1	692	681	9.3	H	11.66 ^e	0.017	2006-09-04	CSJ	900	1.5
UGCA442	Sb	23:43:45.55	-31:57:24.4	267	282	4.27	TRGB ^a	13.58 ^a	0.017	2006-09-04	CSJ	900	1.7
ESO348-G009	Irr	23:49:23.47	-37:46:18.9	648	633	8.7	H	15.83 ^j	0.013	2006-09-03	JSF	1620	2.9
NGC7793	S0	23:57:49.83	-32:35:27.7	229	252	3.91	TRGB ^a	9.70 ^a	0.019	2004-10-24	CSJ	900	2.3

REFERENCES. — (a) Karachentsev et al. 2004; (b) Karachentsev et al. 2006; (c) Seth et al. 2005; (d) Carrasco et al. 2001; (e) ESO-LV catalogue, Lauberts & Valentijn 1989; (f) Makarova et al. 2005; (g) Parodi et al. 2002; (h) Vader & Chaboyer 1994; (i) Karachentseva & Karachentsev 2000; (j) Maddox et al. 1990; (k) Tonry et al. 2001.

(*) This galaxy is listed as HIZOAJ1618-55 in the NASA Extragalactic Database (NED). We use the name of HIZOAJ1616-55 which is the original name listed in Juraszek et al. (2000).

(**) We use KK2000 to indicate that the original listing of this galaxy was in the Karachentseva & Karachentsev (2000) paper and KKS2000 to indicate that it was originally listed in the Karachentsev et al. (2000) paper. This is consistent with the names listed in NED.

(***) The distance estimate for KK2000-04 and KK2000-06 is based on a group membership listed by Karachentseva & Karachentsev (2000). These values are discussed in detail in §5. The distance estimate for KK2000-25 is based on a H I spectra obtained by Huchtmeier et al. (2001). Our new data clearly shows that this value is incorrect.

TABLE 3
GALAXY PARAMETERS: MEASURED

Name (1)	$m_{H,obs}$ (mag) (2)	r_{eff} (arcsec) (3)	$\langle\mu_H\rangle_{eff}$ (mag arcsec $^{-2}$) (4)	e (5)	PA (6)
SC18	14.94 ± 0.05	12.9 ± 0.5	22.50 ± 0.02	0.5	50
ESO349-G031	12.96 ± 0.06	29.4 ± 1.6	22.29 ± 0.04	0.05	0
ESO294-G010	12.4 ± 0.1	19.7 ± 1.4	20.84 ± 0.06	0.3	5
ESO473-G024	13.7 ± 0.1	24.0 ± 2.7	22.6 ± 0.1	0.5	30
SC24	14.8 ± 0.2	16.8 ± 2.6	22.88 ± 0.08	0.5	-5
IC1574	11.89 ± 0.08	30.1 ± 1.7	21.28 ± 0.04	0.6	-10
ESO540-G030	13.0 ± 0.1	30.5 ± 1.7	22.40 ± 0.02	0.05	0
UGCA15	12.73 ± 0.09	32.2 ± 1.6	22.26 ± 0.02	0.7	30
ESO540-G032	13.10 ± 0.08	28.8 ± 1.4	22.39 ± 0.03	0.4	-45
AM0106-382	13.4 ± 0.1	25.0 ± 3.5	22.4 ± 0.2	0.2	45
NGC0625	8.94 ± 0.04	36.3 ± 1.1	18.74 ± 0.03	0.58	-89
SC42	14.13 ± 0.08	10.4 ± 0.9	21.2 ± 0.1	0.5	-5
ESO245-G005	11.1 ± 0.1	49.7 ± 3.4	21.55 ± 0.03	0.38	-53
ESO115-G021	10.71 ± 0.06	33.6 ± 2.0	20.34 ± 0.07	0.7	42
ESO154-G023	10.37 ± 0.07	50.9 ± 2.7	20.90 ± 0.05	0.77	39
NGC1313	6.7 ± 0.3	101.6 ± 15.5	18.74 ± 0.09	0.3	15
NGC1311	10.28 ± 0.08	23.0 ± 1.6	19.09 ± 0.08	0.62	39
AM0319-662	14.00 ± 0.05	21.8 ± 0.7	22.70 ± 0.02	0.1	-50
IC1959	10.84 ± 0.05	20.5 ± 0.7	19.39 ± 0.03	0.7	-30
AM0333-611	13.65 ± 0.08	20.9 ± 1.3	22.26 ± 0.05	0.25	5
IC2038	11.8 ± 0.09	15.8 ± 1.3	19.8 ± 0.1	0.65	-28
IC2039	11.43 ± 0.04	14.1 ± 0.6	19.17 ± 0.06	0.2	-57
NGC1705	10.16 ± 0.07	15.1 ± 1.5	18.1 ± 0.1	0.2	60
NGC1744	9.31 ± 0.09	47.9 ± 3.0	19.70 ± 0.06	0.6	-10
AM0521-343	14.2 ± 0.4	7.1 ± 0.2	20.5 ± 0.4	0.3	-45
KKS2000-55	10.44 ± 0.05	32.5 ± 0.7	20 ± 0	0.55	-60
ESO364-G029	11.92 ± 0.08	35.1 ± 1.8	21.64 ± 0.02	0.6	57
ESO121-G020	13.87 ± 0.09	17.6 ± 1.2	22.10 ± 0.05	0.25	45
ESO308-G022	13.4 ± 0.1	25.0 ± 1.9	22.32 ± 0.07	0.2	-50
KKS2000-09	11.48 ± 0.07	8.4 ± 0.9	18.3 ± 0.1	0.35	25
Argo	12.72 ± 0.08	37.3 ± 1.7	22.57 ± 0.02	0.5	45
ESO059-G001	11.28 ± 0.06	34.4 ± 1.4	20.96 ± 0.03	0.3	-20
AM0737-691	12.2 ± 0.1	32.1 ± 3.3	21.94 ± 0.08	0.2	-30
KK2000-25	11.66 ± 0.05	11.9 ± 0.5	19.03 ± 0.03	0.15	60
ESO006-G001	11.37 ± 0.06	20.0 ± 1.1	19.87 ± 0.06	0.12	-13
UGCA148	12.14 ± 0.05	19.0 ± 0.6	20.53 ± 0.02	0.35	60
NGC2784	6.16 ± 0.07	27.2 ± 2.9	15.3 ± 0.2	0.56	73
KK98-73	13.0 ± 0.1	13.0 ± 0.8	20.57 ± 0.01	0.4	45
UGCA153	12.6 ± 0.2	30.9 ± 3.8	22.0 ± 0.1	0.6	-48
NGC2835	7.1 ± 0.2	88.0 ± 10.2	18.8 ± 0.1	0.3	-20
UGCA162	12.49 ± 0.09	20.8 ± 1.4	21.08 ± 0.06	0.8	30
ESO565-G003	12.79 ± 0.07	16.4 ± 0.8	20.85 ± 0.05	0.25	30
NGC2915	9.53 ± 0.05	21.3 ± 1.1	18.17 ± 0.06	0.4	-53
NGC3115	5.70 ± 0.07	27.3 ± 2.8	14.9 ± 0.2	0.6	44
IC4662	8.71 ± 0.03	33.1 ± 0.7	18.31 ± 0.03	0.34	-80
ESO461-G036	13.9 ± 0.2	14.7 ± 2.2	21.7 ± 0.1	0.4	25
DDO210	12.30 ± 0.09	47.0 ± 1.7	22.65 ± 0.01	0.4	-80
IC5052	8.89 ± 0.05	54.9 ± 1.8	19.6 ± 0.03	0.85	-40
IC5152	8.26 ± 0.03	53.5 ± 1.5	18.90 ± 0.03	0.35	-85
ESO468-G020	13.2 ± 0.1	21.4 ± 1.0	21.85 ± 0.04	0.4	25
UGCA438	11.2 ± 0.1	36.1 ± 2.5	20.96 ± 0.05	0.2	-40
IC5332	8.14 ± 0.03	68.62 ± 1.5	19.32 ± 0.02	0.05	0
ESO347-G017	11.78 ± 0.08	21.8 ± 1.6	20.47 ± 0.09	0.65	-85
NGC7713	8.45 ± 0.06	44.0 ± 2.3	18.66 ± 0.06	0.55	-10
UGCA442	11.27 ± 0.07	32.5 ± 1.8	20.82 ± 0.05	0.75	53
ESO348-G009	12.66 ± 0.09	30.5 ± 1.7	22.08 ± 0.03	0.6	75
NGC7793	6.5 ± 0.1	88.9 ± 5.5	18.27 ± 0.04	0.4	-80

TABLE 4
GALAXY PARAMETERS: DERIVED

Name (1)	r_{eff} (kpc) (2)	μ_0 (mag arcsec $^{-2}$) (3)	n (4)	α (arcsec) (5)	Δm (mag) (6)	R_{eff} (arcsec) (7)	R_{eff} (kpc) (8)	$M_{H,0}$ (mag) (9)	$\log_{10}(M_*)$ ($\log_{10}(M_{\odot})$) (10)
SC18	0.11 ± 0.01	22.11 ± 0.09	2.08 ± 0.3	20.15 ± 1.0	0.18	16.1 ± 1.3	0.14 ± 0.01	-11.5 ± 0.2	5.9 ± 0.2
ESO349-G031	0.46 ± 0.03	21.57 ± 0.4	1.21 ± 0.2	26.80 ± 4.0	0.05	33.7 ± 6.6	0.52 ± 0.09	-14.6 ± 0.2	7.2 ± 0.2
ESO294-G010	0.18 ± 0.02	20.11 ± 0.4	1.10 ± 0.5	18.20 ± 5.8	0.14	26.1 ± 13.1	0.24 ± 0.09	-14.2 ± 0.2	7.0 ± 0.2
ESO473-G024	1.0 ± 0.1	21.63 ± 0.3	1.17 ± 0.3	23.41 ± 6.5	0.28	30.8 ± 11.0	1.2 ± 0.3	-16.1 ± 0.3	7.8 ± 0.2
SC24	0.09 ± 0.02	21.58 ± 0.4	1.98 ± 0.2	12.97 ± 4.6	0.18	22.4 ± 9.6	0.12 ± 0.04	-10.7 ± 0.3	5.6 ± 0.2
IC1574	0.72 ± 0.04	20.54 ± 0.08	1.50 ± 0.1	42.91 ± 2.3	0.01	42.9 ± 3.3	1.02 ± 0.06	-16.6 ± 0.2	8.0 ± 0.2
ESO540-G030	0.50 ± 0.03	21.70 ± 0.4	1.17 ± 0.4	26.77 ± 9.3	0.01	35.2 ± 16.3	0.6 ± 0.2	-14.7 ± 0.2	7.2 ± 0.2
UGC15	0.52 ± 0.03	21.51 ± 0.03	1.49 ± 0.07	54.51 ± 1.2	0.05	54.9 ± 2.1	0.89 ± 0.03	-15.0 ± 0.2	7.3 ± 0.2
ESO540-G032	0.48 ± 0.03	20.89 ± 3.1	0.90 ± 1.7	17.73 ± 19.2	0.15	36.0 ± 84.9	0.6 ± 1.1	-14.7 ± 0.2	7.2 ± 0.2
AM0106-382	1.0 ± 0.1	19.91 ± 0.4	0.56 ± 0.1	3.33 ± 2.3	0.13	27.2 ± 21.0	1.1 ± 0.8	-16.4 ± 0.2	7.9 ± 0.2
NGC0625	0.72 ± 0.03	17.20 ± 0.04	0.82 ± 0.1	23.38 ± 0.8	0.05	58.0 ± 10.5	1.1 ± 0.1	-19.2 ± 0.2	9.0 ± 0.2
SC42	0.04 ± 0.01	18.21 ± 0.6	0.43 ± 0.05	0.75 ± 0.5	0.04	22.5 ± 16.8	0.10 ± 0.03	-10.6 ± 0.2	5.6 ± 0.2
ESO245-G005	1.07 ± 0.08	20.95 ± 0.04	1.46 ± 0.09	61.74 ± 2.3	0.04	63.3 ± 3.6	1.36 ± 0.07	-17.2 ± 0.2	8.2 ± 0.2
ESO115-G021	0.76 ± 0.05	18.81 ± 0.1	0.95 ± 0.08	27.52 ± 3.6	0.09	50.3 ± 7.9	1.1 ± 0.1	-17.7 ± 0.2	8.4 ± 0.2
ESO154-G023	1.39 ± 0.08	19.85 ± 0.03	1.20 ± 0.03	85.02 ± 2.5	0.19	108.1 ± 3.9	3.00 ± 0.06	-18.6 ± 0.2	8.8 ± 0.2
NGC1313	2.0 ± 0.3	16.41 ± 0.2	0.46 ± 0.03	12.69 ± 3.6	0.86	260.6 ± 83.2	5.2 ± 0.7	-22.3 ± 0.4	10.3 ± 0.2
NGC1311	0.61 ± 0.04	17.70 ± 0.06	0.93 ± 0.03	19.30 ± 1.2	0.05	36.7 ± 2.6	0.97 ± 0.04	-18.5 ± 0.2	8.7 ± 0.2
AM0319-662	0.43 ± 0.02	22.19 ± 0.4	1.77 ± 0.8	29.05 ± 6.8	0.06	25.6 ± 8.7	0.5 ± 0.1	-14.2 ± 0.2	7.0 ± 0.2
IC1959	0.63 ± 0.02	18.46 ± 0.08	1.42 ± 0.06	32.04 ± 1.6	0.04	33.7 ± 1.9	1.04 ± 0.04	-18.2 ± 0.2	8.6 ± 0.2
AM0333-611	1.35 ± 0.08	20.69 ± 1.5	0.73 ± 0.3	8.58 ± 6.9	0.31	28.6 ± 28.4	1.8 ± 1.4	-17.3 ± 0.2	8.3 ± 0.2
IC2038	1.3 ± 0.1	17.62 ± 0.2	0.70 ± 0.05	6.32 ± 1.2	0.03	23.7 ± 5.0	1.9 ± 0.3	-19.3 ± 0.2	9.1 ± 0.2
IC2039	1.13 ± 0.05	15.04 ± 0.6	0.37 ± 0.03	0.25 ± 0.2	0.03	20.1 ± 12.9	1.6 ± 0.7	-19.7 ± 0.2	9.2 ± 0.2
NGC1705	0.37 ± 0.04	15.33 ± 0.4	0.44 ± 0.04	0.90 ± 0.4	0.15	23.7 ± 11.6	0.6 ± 0.2	-18.5 ± 0.2	8.8 ± 0.2
NGC1744	1.8 ± 0.1	17.86 ± 0.1	0.69 ± 0.05	21.97 ± 3.6	0.13	86.1 ± 16.7	3.3 ± 0.4	-20.3 ± 0.2	9.5 ± 0.2
AM0521-343	0.36 ± 0.01	—	—	—	—	—	—	-15.9 ± 0.5	7.7 ± 0.3
KKS2000-55	1.59 ± 0.04	18.05 ± 0.4	0.63 ± 0.09	11.36 ± 4.5	0.15	59.6 ± 27.1	2.9 ± 0.7	-20.2 ± 0.2	9.4 ± 0.2
ESO364-G029	1.30 ± 0.07	21.11 ± 0.05	1.78 ± 0.1	60.81 ± 2.2	0.02	53.3 ± 2.7	1.94 ± 0.07	-17.5 ± 0.2	8.3 ± 0.2
ESO121-G020	0.52 ± 0.04	20.82 ± 0.8	0.95 ± 0.4	12.22 ± 5.9	0.19	22.3 ± 14.0	0.7 ± 0.3	-15.3 ± 0.2	7.4 ± 0.2
ESO308-G022	0.92 ± 0.07	20.87 ± 0.3	0.71 ± 0.2	10.76 ± 5.2	0.53	38.8 ± 22.8	1.4 ± 0.5	-16.7 ± 0.2	8.0 ± 0.2
KKS2000-09	0.26 ± 0.03	14.12 ± 4.6	0.42 ± 0.2	0.28 ± 1.8	0.06	9.7 ± 63.4	0.3 ± 1.7	-17.9 ± 0.2	8.5 ± 0.2
Argo	0.89 ± 0.04	21.87 ± 0.1	1.32 ± 0.2	48.77 ± 4.6	0.27	55.4 ± 7.7	1.3 ± 0.1	-16.1 ± 0.2	7.8 ± 0.2
ESO059-G001	0.76 ± 0.04	20.23 ± 0.2	1.33 ± 0.2	36.68 ± 6.2	0.1	41.3 ± 8.3	0.9 ± 0.2	-17.2 ± 0.2	8.2 ± 0.2
AM0737-691	2.5 ± 0.3	20.67 ± 0.2	1.07 ± 0.2	21.41 ± 3.9	0.1	32.0 ± 7.1	2.5 ± 0.6	-19.0 ± 0.3	9.0 ± 0.2
KK2000-25	0.03 ± 0.01	18.13 ± 0.08	1.12 ± 0.03	9.41 ± 0.5	0.03	13.1 ± 0.7	0.03 ± 0.01	-11.9 ± 0.2	6.1 ± 0.2
ESO006-G001	0.65 ± 0.04	19.20 ± 0.5	1.07 ± 0.2	16.11 ± 5.2	0.08	24.1 ± 8.9	0.8 ± 0.2	-17.8 ± 0.2	8.5 ± 0.2
UGC148	0.90 ± 0.03	19.85 ± 0.07	1.37 ± 0.09	22.15 ± 1.3	0.05	24.2 ± 1.9	1.15 ± 0.07	-18.0 ± 0.2	8.5 ± 0.2
NGC2784	1.3 ± 0.1	15.26 ± 0.4	0.82 ± 0.1	26.85 ± 9.0	0.04	66.6 ± 24.4	3.2 ± 0.5	-24.0 ± 0.2	10.9 ± 0.2
KK98-73	0.62 ± 0.04	19.48 ± 0.3	0.95 ± 0.1	10.74 ± 2.2	0.36	19.6 ± 4.8	0.9 ± 0.1	-17.4 ± 0.2	8.3 ± 0.2
UGC153	1.0 ± 0.1	20.93 ± 0.2	1.15 ± 0.1	33.31 ± 5.2	0.11	44.8 ± 8.5	1.5 ± 0.2	-16.7 ± 0.3	8.0 ± 0.2
NGC2835	3.5 ± 0.4	16.50 ± 0.04	0.52 ± 0.01	14.27 ± 0.8	0.54	160.0 ± 10.7	6.4 ± 0.2	-23.1 ± 0.3	10.6 ± 0.2
UGC162	0.77 ± 0.05	20.22 ± 0.02	1.35 ± 0.02	47.70 ± 0.7	0.32	52.9 ± 1.0	2.00 ± 0.02	-17.3 ± 0.2	8.3 ± 0.2
ESO565-G003	0.60 ± 0.03	19.97 ± 0.5	1.01 ± 0.2	12.69 ± 4.1	0.05	20.8 ± 7.6	0.8 ± 0.2	-16.7 ± 0.2	8.0 ± 0.2
NGC2915	0.39 ± 0.02	15.97 ± 0.2	0.63 ± 0.03	5.21 ± 0.8	0.03	27.4 ± 4.8	0.50 ± 0.07	-18.6 ± 0.2	8.8 ± 0.2
NGC3115	1.3 ± 0.1	10.20 ± 0.4	0.31 ± 0.02	0.18 ± 0.1	0.14	62.1 ± 43.4	3.0 ± 0.9	-24.4 ± 0.2	11.1 ± 0.2
IC4662	0.39 ± 0.02	17.27 ± 0.2	0.94 ± 0.05	22.68 ± 2.9	0.03	42.3 ± 5.8	0.50 ± 0.06	-18.3 ± 0.2	8.7 ± 0.2
ESO461-G036	0.56 ± 0.08	21.16 ± 0.2	1.80 ± 0.4	21.07 ± 2.8	0.14	18.3 ± 3.4	0.7 ± 0.1	-15.9 ± 0.3	7.7 ± 0.2
DDO210	0.21 ± 0.02	22.07 ± 0.08	1.52 ± 0.2	64.49 ± 4.7	0.27	63.8 ± 6.4	0.29 ± 0.03	-12.9 ± 0.2	6.5 ± 0.2
IC5052	1.61 ± 0.06	18.07 ± 0.02	1.27 ± 0.02	88.82 ± 1.4	0.28	105.4 ± 2.1	3.08 ± 0.04	-20.3 ± 0.2	9.5 ± 0.2
IC5152	0.54 ± 0.03	17.65 ± 0.08	0.96 ± 0.04	35.44 ± 2.7	0.01	63.5 ± 5.5	0.64 ± 0.05	-18.3 ± 0.2	8.7 ± 0.2
ESO468-G020	0.41 ± 0.02	21.13 ± 0.07	1.28 ± 0.1	24.93 ± 1.9	0.13	29.3 ± 3.0	0.55 ± 0.04	-14.9 ± 0.2	7.3 ± 0.2
UGC438	0.39 ± 0.03	20.49 ± 0.2	1.31 ± 0.08	38.34 ± 3.4	0.03	43.9 ± 4.4	0.47 ± 0.04	-15.6 ± 0.2	7.6 ± 0.2
IC5332	3.19 ± 0.08	16.92 ± 0.2	0.52 ± 0.04	8.51 ± 2.4	0.21	95.4 ± 30.5	4.4 ± 1.0	-22.0 ± 0.2	10.1 ± 0.2
ESO347-G017	1.00 ± 0.07	18.19 ± 0.4	0.74 ± 0.08	9.02 ± 2.9	0.22	29.0 ± 10.3	1.3 ± 0.4	-18.3 ± 0.2	8.7 ± 0.2
NGC7713	2.0 ± 0.1	16.98 ± 0.2	0.83 ± 0.06	24.46 ± 3.8	0.02	59.0 ± 10.6	2.7 ± 0.4	-21.4 ± 0.2	9.9 ± 0.2

TABLE 4
GALAXY PARAMETERS: DERIVED

UGCA442	0.67 ± 0.04	19.94 ± 0.03	1.42 ± 0.04	57.38 ± 1.5	0.44	60.4 ± 2.0	1.25 ± 0.03	-17.3 ± 0.2	8.3 ± 0.2
ESO348-G009	1.28 ± 0.07	21.26 ± 0.05	1.31 ± 0.07	44.50 ± 2.0	0.15	51.0 ± 3.1	2.14 ± 0.08	-17.2 ± 0.2	8.2 ± 0.2
NGC7793	1.7 ± 0.1	16.47 ± 0.08	0.62 ± 0.02	28.72 ± 3.0	0.46	159.4 ± 18.7	3.0 ± 0.2	-21.9 ± 0.2	10.1 ± 0.2